Published for SISSA by Springer

Received: May 2, 2024
Accepted: June 25, 2024
Published: July 25, 2024

Virtual QCD corrections to $gg \to ZZ$: top-quark loops from a transverse-momentum expansion

Giuseppe Degrassi[a], **Ramona Gröber**[b] **and Marco Vitti**[c,d]

[a] *Dipartimento di Matematica e Fisica, Università di Roma Tre and INFN, sezione di Roma Tre, Via della Vasca Navale 84, I-00146 Rome, Italy*

[b] *Dipartimento di Fisica e Astronomia 'G. Galilei', Università di Padova and INFN, sezione di Padova, Via Francesco Marzolo 8, I-35131 Padova, Italy*

[c] *Institute for Theoretical Particle Physics, Karlsruhe Institute of Technology (KIT), Wolfgang-Gaede Straße 1, D-76128 Karlsruhe, Germany*

[d] *Institute for Astroparticle Physics, Karlsruhe Institute of Technology (KIT), Hermann-von-Helmholtz-Platz 1, D-76344 Eggenstein-Leopoldshafen, Germany*

E-mail: giuseppe.degrassi@uniroma3.it, ramona.groeber@pd.infn.it, marco.vitti@kit.edu

Abstract: We present the virtual corrections due to the top-quark loops for the process $gg \to ZZ$ at next-to-leading order in QCD. The associated two-loop box diagrams are computed using a small-transverse-momentum expansion. Our results are then merged with those available in the complementary energy region, obtained via a high-energy expansion, in order to provide an analytic result that is valid in the whole phase space. The results presented allow for an efficient modelling of the signal-background interference as well as the irreducible background in off-shell Higgs production.

Keywords: Higher-Order Perturbative Calculations, Higgs Production, Higgs Properties

ArXiv ePrint: 2404.15113

https://doi.org/10.1007/JHEP07(2024)244

Contents

1 Introduction

The quest for the determination of the properties of the Higgs boson, after its discovery at the LHC, has been very rewarding. While the main Higgs production channels have been established and new challenging decay modes are being studied (see e.g. refs. [1, 2]), a large variety of measurements have entered the precision domain, requiring improved predictions for Higgs-related processes within the Standard Model (SM) [3, 4]. A significant role in this program is played by the production of a pair of Z bosons, $pp \to ZZ$, which has been one of the discovery channels of the Higgs and today is important both as a probe of the electroweak (EW) symmetry breaking and for precision Higgs physics [5, 6].

In the theoretical SM prediction of $pp \to ZZ$ production two partonic sub-processes have to be considered. The first one is quark-antiquark annihilation, $q\bar{q} \to ZZ$, which gives the largest contribution to the hadronic cross section. The leading-order (LO) amplitude for this channel is related to purely EW tree-level diagrams [7], and corrections through next-to-next-to-leading order (NNLO) in QCD [8–13] and through next-to-leading order (NLO) in the EW theory [14–16] are available. The second partonic contribution, which is the main topic of this paper, comes from the gluon-initiated channel, $gg \to ZZ$. The gluon-initiated channel at LO is associated to one-loop diagrams, which contribute as an important $\mathcal{O}(\alpha_s^2)$ correction, accounting for about 10% of the hadronic cross section at NNLO for $\sqrt{s} = 13\,\text{TeV}$ [17].

The one-loop diagrams for $gg \to ZZ$ at LO have been computed for the first time in refs. [18, 19]. They feature two topologies: the triangles (see figure 1(a)) are associated to Higgs production via the sub-process $gg \to H \to ZZ$, while the box diagrams (figure 1(b)) are related to the process of non-resonant (a.k.a. *continuum*) ZZ production, which constitutes

JHEP07(2024)244

an irreducible background in experimental Higgs searches. Moreover, continuum production plays a relevant role in the indirect determination of the Higgs total decay width, Γ_H [20, 21]. Indeed, in refs. [22, 23] it has been suggested that upper limits on Γ_H can be obtained from the investigation of the invariant-mass distribution of the two Z bosons system, M_{ZZ}, away from the region where the Higgs is produced on shell[1] [28]. Under the assumption that no beyond-SM physics spoils the known correlation between on- and off-shell amplitudes [29, 30], the latest experimental measurements could exclude, for the first time, deviations in Γ_H below $\mathcal{O}(100\%)$ from its SM prediction [31, 32].

In this situation, a good theoretical control over the destructive interference between the Higgs-mediated and continuum amplitudes is crucial. This motivates the inclusion of NLO QCD corrections to the gluon-initiated channel. The NLO corrections to the Higgs-mediated diagrams are known exactly, adapting results for the production of a single Higgs with virtuality M_{ZZ} [33–35]. Concerning the continuum term, exact analytic results for the related two-loop box integrals have been obtained in the case of loops of massless quarks [36, 37]. We remark that, at the level of the inclusive $gg \to ZZ$ cross section, the contribution from light quarks is the dominant one, and furthermore it constitutes more than 50% of the $\mathcal{O}(\alpha_s^2)$ corrections to ZZ production [10, 17].

The top-quark contribution to continuum $gg \to ZZ$ starts to become relevant for invariant masses in the range $M_{ZZ} > 2m_Z$ and it is expected to be substantial in the region where M_{ZZ} is larger than twice the mass of the top, m_t. At present, the top-quark contribution is not known in full analytic form, as the scale associated to the mass of the heavy quark complicates the calculation of the two-loop box integrals. Several approximate analytic evaluations of this contribution have been discussed in the literature. The large-mass expansion (LME) has been used in refs. [38–40] to obtain reliable predictions in the region $2\,m_Z < M_{ZZ} \lesssim 2\,m_t$. In ref. [40] an improvement of the LME results by means of conformal mapping and Padé approximants has also been studied. A further improvement of the LME via an expansion around the top threshold has been presented in ref. [41]. Analytic predictions that are reliable for large invariant masses have been obtained using the so-called High-Energy (HE) expansion [42]. Still, the latter approach is expected to break down in the region $M_{ZZ} \lesssim 750\,\text{GeV}$, and in ref. [42] Padé approximants were used in order to improve the expansion. Finally, exact results based on numerical approaches have been obtained in refs. [43, 44], showing good agreement with ref. [42] in the ranges of small or large invariant masses. Very recently, the numerical results of ref. [43] have been used to compute the full NLO QCD corrections to $gg \to ZZ$ [45].

In this paper, we present the computation of the contribution from top-quark loops to the virtual NLO QCD corrections to $gg \to ZZ$. In the calculation we employ an expansion in the transverse momentum of the Z, p_T, following refs. [46, 47]. Our first goal is to provide an accurate approximation of the virtual QCD corrections that can be valid in the invariant-mass region that so far has not been covered by any of the analytic approaches discussed above, namely the region $350 \lesssim M_{ZZ} \lesssim 750\,\text{GeV}$. Since the p_T expansion "contains" the LME result, the region of validity of our approach is actually given by $2\,m_Z < M_{ZZ} \lesssim 750\,\text{GeV}$.

Furthermore, it has been previously shown that an expansion in the forward kinematics [48, 49], like the p_T expansion, and the HE expansion can be combined in order to approximate

[1] Off-shell Higgs production can also provide an excellent probe of new physics, for instance of light-quark Yukawa couplings [24], modified trilinear Higgs self-coupling [25] or Higgs portal models [26, 27].

JHEP07(2024)244

the two-loop box amplitudes with good accuracy over the whole phase space. In the second part of the paper, then, we show that this can be done also for $gg \to ZZ$, and we discuss the combination of our new results with those of ref. [42].

The paper is organized as follows. In section 2 we set the notation and we comment on the application of the p_T expansion to the $gg \to ZZ$ case. The next section is devoted to a comparison between the known LO amplitude and our approximation. In section 4 we then consider the application of the p_T expansion at NLO and discuss how our p_T-expanded results can be merged with those derived via the HE expansion. Section 5 contains our NLO results, and we present our conclusions in section 6. The paper is complemented by two appendices. In appendix A we report the explicit expressions for the projectors we employ in the calculation. We present also the relation between our form factors and the ones used in ref. [42]. In appendix B we report the exact results for the NLO triangle and the reducible double-triangle contributions.

2 Definitions and the p_T-expansion method

2.1 Definitions

We consider the process $g_a^\mu(p_1) g_b^\nu(p_2) \to Z^\rho(-p_3) Z^\sigma(-p_4)$. The amplitude can be defined as

$$\mathcal{A} = \sqrt{2} m_Z^2 G_F \, \frac{\alpha_s(\mu_R)}{\pi} \delta_{ab} \, \epsilon_\mu^a(p_1) \epsilon_\nu^b(p_2) \epsilon_\rho^*(p_3) \epsilon_\sigma^*(p_4) \, \hat{\mathcal{A}}^{\mu\nu\rho\sigma}(p_1, p_2, p_3), \tag{2.1}$$

where G_F is the Fermi constant, $\alpha_s(\mu_R)$ is the strong coupling constant evaluated at a renormalisation scale μ_R and the polarization vectors of the gluons and the Z bosons are $\epsilon_\mu^a(p_1), \epsilon_\nu^b(p_2)$ and $\epsilon_\rho(p_3), \epsilon_\sigma(p_4)$, respectively. The Lorentz structure of the amplitude is encoded in the tensor $\hat{\mathcal{A}}^{\mu\nu\rho\sigma}(p_1, p_2, p_3)$, whose most general decomposition consists of 138 parity-even Lorentz structures. However, by imposing the transversality of the external polarization vectors w.r.t. the relative four-momentum

$$\epsilon(p_i) \cdot p_i = 0 \qquad i = 1, \ldots, 4, \tag{2.2}$$

and by fixing the gauge of the external gluons with

$$\epsilon(p_1) \cdot p_2 = 0 \qquad \epsilon(p_2) \cdot p_1 = 0, \tag{2.3}$$

$\hat{\mathcal{A}}^{\mu\nu\rho\sigma}$ can be written as a linear combination of 20 Lorentz structures [36, 42, 50]

$$\hat{\mathcal{A}}^{\mu\nu\rho\sigma}(p_1, p_2, p_3) = \sum_{i=1}^{20} S_i^{\mu\nu\rho\sigma} f_i(\hat{s}, \hat{t}, \hat{u}, m_t, m_Z), \tag{2.4}$$

where the scalar form factors f_i depend, besides m_t and m_Z, on the partonic Mandelstam variables.[2] Assuming all momenta to be incoming, the latter are defined as

$$\hat{s} = (p_1 + p_2)^2, \quad \hat{t} = (p_1 + p_3)^2, \quad \hat{u} = (p_2 + p_3)^2 \tag{2.5}$$

[2]The Higgs mediated diagrams (see figure 1(a) and figure 2(a,b)) depend also on the Higgs mass.

JHEP07(2024)244

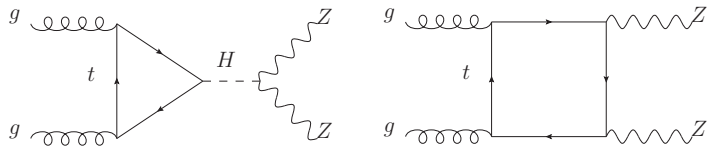

Figure 1. Representative Feynman diagrams contributing to the $gg \to ZZ$ amplitude at LO. Only the contribution from top-quark loops is shown.

and the relation $\hat{s} + \hat{t} + \hat{u} = 2\,m_Z^2$ is satisfied. We checked that the Lorentz structures that give a nonzero contribution to the amplitude are

$$\begin{aligned}
S_1^{\mu\nu\rho\sigma} &= g^{\mu\nu} g^{\rho\sigma} & S_2^{\mu\nu\rho\sigma} &= g^{\mu\rho} g^{\nu\sigma} & S_3^{\mu\nu\rho\sigma} &= g^{\mu\sigma} g^{\nu\rho} & S_4^{\mu\nu\rho\sigma} &= p_1^\rho p_3^\nu g^{\mu\sigma} \\
S_5^{\mu\nu\rho\sigma} &= p_2^\rho p_3^\nu g^{\mu\sigma} & S_6^{\mu\nu\rho\sigma} &= p_1^\rho p_3^\mu g^{\nu\sigma} & S_7^{\mu\nu\rho\sigma} &= p_2^\rho p_3^\mu g^{\nu\sigma} & S_8^{\mu\nu\rho\sigma} &= p_3^\mu p_3^\nu g^{\rho\sigma} \\
S_9^{\mu\nu\rho\sigma} &= p_1^\rho p_1^\sigma g^{\mu\nu} & S_{10}^{\mu\nu\rho\sigma} &= p_1^\rho p_2^\sigma g^{\mu\nu} & S_{11}^{\mu\nu\rho\sigma} &= p_1^\sigma p_2^\rho g^{\mu\nu} & S_{12}^{\mu\nu\rho\sigma} &= p_2^\rho p_2^\sigma g^{\mu\nu} \\
S_{13}^{\mu\nu\rho\sigma} &= p_1^\sigma p_3^\nu g^{\mu\rho} & S_{14}^{\mu\nu\rho\sigma} &= p_2^\sigma p_3^\nu g^{\mu\rho} & S_{15}^{\mu\nu\rho\sigma} &= p_1^\sigma p_3^\mu g^{\nu\rho} & S_{16}^{\mu\nu\rho\sigma} &= p_2^\sigma p_3^\mu g^{\nu\rho} \\
S_{17}^{\mu\nu\rho\sigma} &= p_1^\rho p_1^\sigma p_3^\mu p_3^\nu & S_{18}^{\mu\nu\rho\sigma} &= p_1^\rho p_2^\sigma p_3^\mu p_3^\nu & S_{19}^{\mu\nu\rho\sigma} &= p_1^\sigma p_2^\rho p_3^\mu p_3^\nu & S_{20}^{\mu\nu\rho\sigma} &= p_2^\rho p_2^\sigma p_3^\mu p_3^\nu
\end{aligned} \tag{2.6}$$

where we follow the numbering of ref. [42].

In order to simplify the evaluation of the cross section, in our work we express the amplitude in terms of a set of orthonormal projectors

$$\hat{\mathcal{A}}^{\mu\nu\rho\sigma}(p_1, p_2, p_3) = \sum_{i=1}^{20} \mathcal{P}_i^{\mu\nu\rho\sigma} \mathcal{A}_i(\hat{s}, \hat{t}, \hat{u}, m_t, m_Z), \tag{2.7}$$

where the tensors $\mathcal{P}_i^{\mu\nu\rho\sigma}$ are constructed as linear combinations of the Lorentz structures defined in eqs. (2.6), using a Gram-Schmidt procedure for the orthogonalization. In appendix A we give the explicit expressions for the projectors. Here we point out that, to efficiently perform the p_T expansion [47], we choose the projectors to be either symmetric or anti-symmetric under the interchange $\{\mu \leftrightarrow \nu, p_1 \leftrightarrow p_2\}$. This choice also allows to reduce the number of relevant form factors[3] from 20 to 16. We present our results in terms of the $\mathcal{A}_i$ form factors of eq. (2.7), while in appendix A we include the relations to obtain the latter as a combination of the f_i in eqs. (2.4).

We consider a perturbative expansion of the form factors in the strong coupling

$$\mathcal{A}_i = \mathcal{A}_i^{(0)} + \frac{\alpha_s}{\pi} \mathcal{A}_i^{(1)} + \mathcal{O}(\alpha_s^2) \tag{2.8}$$

where one- and two-loop diagrams contribute respectively to the LO ($\mathcal{A}_i^{(0)}$) and NLO ($\mathcal{A}_i^{(1)}$). According to the topology of the relevant Feynman diagrams (see figure 1), we identify a triangle and a box contribution to the LO form factors

$$\mathcal{A}_i^{(0)} = \mathcal{A}_i^{(0,\triangle)} + \mathcal{A}_i^{(0,\square)}. \tag{2.9}$$

[3] In fact, we observed that enforcing the additional Bose symmetry $\{\rho \leftrightarrow \sigma, p_3 \leftrightarrow p_4\}$ further reduces the relevant form factors to 12. While this may be used for improving the practical implementation of our results, in this paper we use the 16 form factors.

JHEP07(2024)244

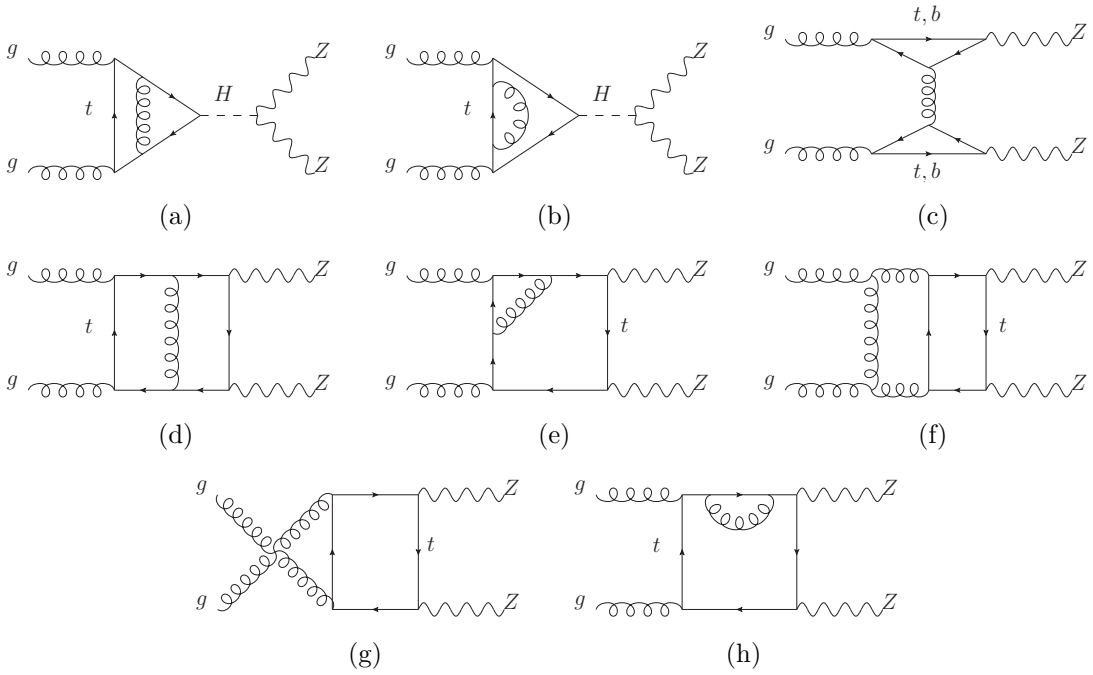

Figure 2. Representative Feynman diagrams contributing to the $gg \to ZZ$ amplitude at NLO. Loops of bottom quarks are included only in the double-triangle diagrams (c).

The above classification is modified at NLO, where the two-loop triangle and box topologies (see figure 2) are supplemented with one-particle-reducible double-triangle diagrams as in figure 2(c). Therefore the NLO form factors are defined as

$$\mathcal{A}_i^{(1)} = \mathcal{A}_i^{(1,\triangle)} + \mathcal{A}_i^{(1,\square)} + \mathcal{A}_i^{(1,\bowtie)}. \tag{2.10}$$

The main result of this paper is the evaluation of the $\mathcal{A}_i^{(1,\square)}$ using the p_T expansion, which is described below. For completeness, we provide also the results for $\mathcal{A}_i^{(1,\triangle)}$ and $\mathcal{A}_i^{(1,\bowtie)}$. We notice that only for $\mathcal{A}_i^{(1,\bowtie)}$ we include the contributions from loops of bottom as well as top quarks, since the whole fermion generation must be considered to remove the axial anomaly.

With the previous definitions, the partonic cross section at LO is expressed as

$$\hat{\sigma}^{(0)}(\hat{s}) = \frac{m_Z^4 G_F^2}{512\pi\hat{s}^2}\left(\frac{\alpha_s(\mu_R)}{\pi}\right)^2 \int_{\hat{t}^-}^{\hat{t}^+} d\hat{t} \sum_i \left|\mathcal{A}_i^{(0)}\right|^2 \tag{2.11}$$

with $\hat{t}^{\pm} = 1/2\left[-\hat{s} + 2m_Z^2 \pm \sqrt{\hat{s}^2 - \hat{s}\ 4m_Z^2}\right]$.

2.2 The p_T-expansion method

We now briefly recall the main points of the p_T expansion. The details of the method are presented in refs. [46, 47]. The Feynman amplitude is expanded in the transverse momentum at the integrand level via the introduction of the vector $r^\mu = p_1^\mu + p_3^\mu$, which satisfies the relations

$$r^2 = \hat{t} \qquad r \cdot p_1 = t' \qquad r \cdot p_2 = -t' \tag{2.12}$$

JHEP07(2024)244

and can be written as

$$r^\mu = \frac{t'}{s'}(p_2 - p_1)^\mu + r_\perp^\mu, \tag{2.13}$$

where the space-like vector $r_\perp^\mu$ is such that

$$r_\perp \cdot p_1 = r_\perp \cdot p_2 = 0, \qquad r_\perp^2 = -p_T^2, \tag{2.14}$$

with

$$p_T^2 = \frac{\hat{t}\hat{u} - m_Z^4}{\hat{s}}. \tag{2.15}$$

In eqs. (2.12), (2.13) we introduce the primed Mandelstam variables

$$s' = p_1 \cdot p_2 = \frac{\hat{s}}{2}, \quad t' = p_1 \cdot p_3 = \frac{\hat{t} - m_Z^2}{2}, \quad u' = p_2 \cdot p_3 = \frac{\hat{u} - m_Z^2}{2}, \tag{2.16}$$

such that

$$s' + t' + u' = 0, \qquad p_T^2 = \frac{2t'u'}{s'} - m_Z^2. \tag{2.17}$$

The above relations allow to rewrite t' as

$$t' = -\frac{s'}{2}\left\{1 \pm \sqrt{1 - 2\frac{p_T^2 + m_Z^2}{s'}}\right\}. \tag{2.18}$$

We are interested in the expansion of the amplitude in the forward limit, corresponding to $t' \sim 0$, i.e the minus-sign case in eq. (2.18). As discussed in refs. [46, 47], the forward expansion is sufficient to obtain the correct result for the cross section, if the (anti-)symmetry of the form factors with respect to the exchange $t' \leftrightarrow u'$ is ensured. The region of validity of the expansion is given by the condition $p_T^2/(4\,m_t^2) \lesssim 1$.

The p_T expansion of the relevant Feynman diagrams returns a result in terms of the ratios of small vs large quantities, x/y, where $x \in \{p_T^2, m_Z^2\}$ and $y \in \{\hat{s}, m_t^2\}$. We notice that, in the p_T expansion, the transverse momentum and m_Z are treated on the same footing, i.e. a term $\mathcal{O}(p_T^2/m_Z^2)$ is assumed to be $\mathcal{O}(1)$, not to be $\mathcal{O}(p_T^2)$. Therefore the expansion can be also considered in terms of the quantities m_Z^2 and of the combination $p_T^2 + m_Z^2$ that enters in t' (see eq. (2.18)).

After the scalar form factors $\mathcal{A}_i$ are expanded in the small parameters above, and after the scalar integrals are decomposed along a basis of master integrals (MI) using Integration-by-Parts (IBP) identities, the form factors can be written as the following series

$$\mathcal{A}_i = \mathcal{N}(p_T^2, m_Z^2) \sum_{N=0}^{\infty} \sum_{i+j=N} c_{ij} (p_T^2)^i (m_Z^2)^j, \tag{2.19}$$

where the c_{ij} coefficients are linear combinations of the MIs resulting from the IBP reduction, which in turn depend only on $\hat{s}$ and m_t^2, while $\mathcal{N}(p_T^2, m_Z^2)$ is an overall normalization factor which may depend on p_T^2 and m_Z^2.

JHEP07(2024)244

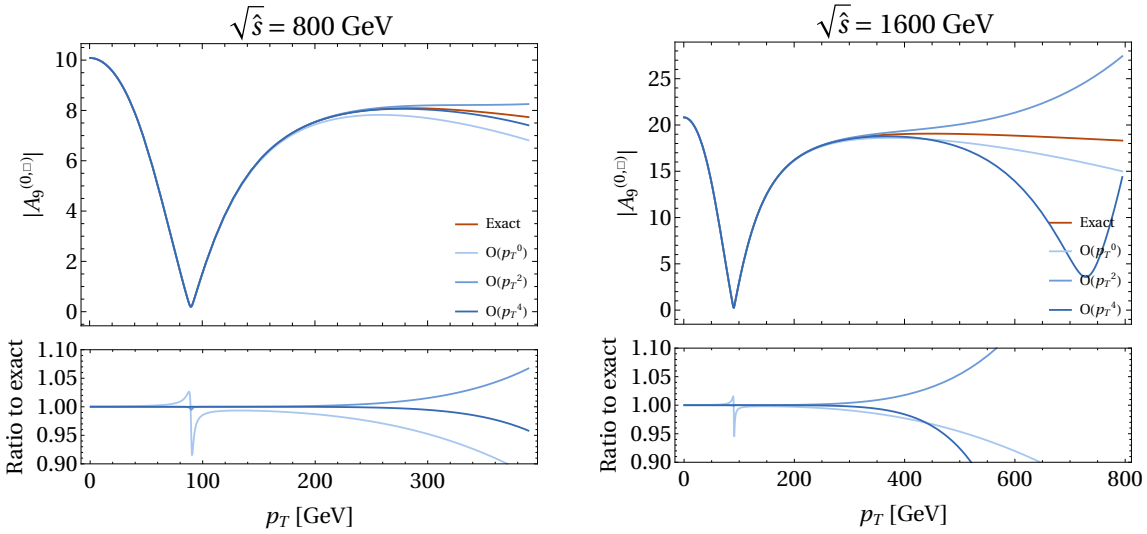

(a) (b)

Figure 3. Absolute value of the form factor $\mathcal{A}_9^{(0,\square)}$ for moderate (a) and high (b) partonic centre-of-mass energies as a function of the transverse momentum. The exact result and the results obtained at various orders in the p_T expansion are shown.

3 Validation of the p_T expansion at LO

In this section we assess the level of accuracy of the p_T expansion in reproducing the known exact result at LO. We used `FeynArts` [51] to generate the relevant amplitudes, which we expanded in the limit of small p_T using private code. The latter relies on several functions implemented in `FeynCalc` [52, 53]. The expanded amplitude has been decomposed along a basis of MIs with `LiteRed` [54, 55]. The MIs can be expressed in terms of the B_0 and C_0 Passarino-Veltman functions [56] of argument m_t^2 and $\hat{s}$ or $-\hat{s}$. We also used `FeynCalc` to recompute the exact LO result for the amplitude and found it in agreement[4] with the one provided in ref. [42]. Since at NLO only the box contributions will be computed in an approximate way via the p_T expansion, in the following we focus on the results of the box form factors, $\mathcal{A}_i^{(0,\square)}$. In particular, we consider the absolute value of the form factor $\mathcal{A}_9^{(0,\square)}$ which provides the largest contribution to the cross section. We notice that the $\mathcal{P}_9^{\mu\nu\rho\sigma}$ projector, as well as others, exhibits a $\mathcal{O}(p_T^{-2})$ term (see eq. (A.9)) that can question the fact that the corresponding form factor, $\mathcal{A}_9^{(0,\square)}$, must be regular in the limit $p_T \to 0$. However, the $\mathcal{O}(p_T^{-2})$ terms that appear in the projectors are always multiplied by combination of the $S_i^{\mu\nu\rho\sigma}$ ($i = 17, 18, 19, 20$) Lorentz structures that, once the gauge condition eq. (2.3) is enforced, exhibit an $r_\perp^\mu\, r_\perp^\nu$ dependence. This dependence ensures that the form factors are regular in the limit $p_T \to 0$.

In figure 3 we plot the exact result for the $\mathcal{A}_9^{(0,\square)}$ form factor, compared to various p_T-expanded results for two values of the partonic centre-of-mass energy. The expanded-over-exact ratio in the bottom parts of the figure shows that the convergence of the expansion is

[4]The comparison has been done for each form factor, using the conversion formulas listed in eqs. (A.21)–(A.38) in appendix A.

JHEP07(2024)244

M_{ZZ}(GeV)	$\hat{\sigma}^{(0)}$(fb)			
	$\mathcal{O}(p_T^0)$	$\mathcal{O}(p_T^2)$	$\mathcal{O}(p_T^4)$	Exact
250	0.12486	0.12418	0.12412	0.12412
345	0.26619	0.26460	0.26448	0.26447
475	0.44887	0.44387	0.44368	0.44367
659	0.43135	0.38051	0.38644	0.38509
808	0.44108	0.30622	0.34712	0.32024
1255	0.70815	1.0303	0.66139	0.1883

Table 1. The partonic LO cross section as a function of M_{ZZ}. The exact result and the ones obtained at various orders in the p_T expansion are shown.

rather fast and that already the $\mathcal{O}(p_T^2)$ result can reproduce the exact one with an accuracy below the percent level. The spikes that are visible in the expanded-over-exact ratio are due to the fact that the form factor is zero near $p_T \sim 100\,\text{GeV}$, and the ratio is not numerically stable. From a comparison between figures 3(a) and 3(b) we observe that, independently on the value of $\sqrt{\hat{s}}$ the expansion is convergent only for values $p_T \lesssim 300\,\text{GeV}$. This is consistent with the limit $p_T^2 \lesssim 4\,m_t^2$ that is assumed in the expansion.

In table 1 we present the values of the LO partonic cross section for $gg \to ZZ$ as a function of the invariant mass of the two Z bosons system. The exact result is compared to various orders in the p_T expansion. The triangle contribution (see figure 1(a)) is evaluated always exactly. The value of the strong coupling is fixed at $\alpha_s = 0.118$, while we use as other parameters $G_F = 1.1663786 \cdot 10^{-5}\ \text{GeV}^{-2}, m_H = 125.1\ \text{GeV}, m_Z = 91.1876\ \text{GeV}, m_t = 173.21\ \text{GeV}$. The table shows that for $M_{ZZ} \lesssim 500\,\text{GeV}$ already the $\mathcal{O}(p_T^2)$ term is in agreement with the exact result at the level of less than 1 per mille. Increasing M_{ZZ} up to 650 GeV the agreement between the exact and the p_T-expanded result starts to deteriorate reaching a ~ 1 per cent difference. However, the inclusion of the $\mathcal{O}(p_T^4)$ term brings back the difference to a few per mille level. For higher values of M_{ZZ} the most important contributions to the cross section come from regions in the phase space where the p_T expansion is not valid and the agreement between the exact and the p_T-expanded results is poor.

4 Virtual corrections at NLO

Having showed that the p_T expansion can provide accurate results for the LO contribution, we move now to discuss its application to the NLO QCD corrections, see figure 2 for representative Feynman diagrams. In fact, we are going to use the p_T expansion only for the evaluation of the two-loop box diagrams. For the two-loop one-particle-irreducible triangles we have adapted the full analytic results of ref. [34], while the reducible double triangles have been computed exactly using `FeynCalc` and checked with the results of ref. [40]. With reference to eq. (2.10), we list the results for the form factors $\mathcal{A}_i^{(1,\triangle)}$ and $\mathcal{A}_i^{(1,\bowtie)}$ in appendix B.

4.1 Box diagrams

The evaluation of the two-loop box diagrams was carried out as follows. We generated the diagrams with `FeynArts` and performed all the manipulations of the amplitude within

JHEP07(2024)244

$\lambda_1\lambda_2\lambda_3\lambda_4$	Numerical	$\mathcal{O}(p_T^4)$
$++++$	3.15549(8) + i 0.47235(8)	3.16038 + i 0.46980
$+++-$	0.15950(7) + i 0.14052(8)	0.16305 + i 0.13885
$+-+-$	-0.38609(7) + i 0.10539(7)	-0.38617 + i 0.11085
$-+++$	-0.46990(8) + i 0.40207(8)	-0.46956 + i 0.40506
$+++0$	1.1248(2) - i 0.0805(2)	1.1256 - i 0.0811
$+-+0$	-1.4803(2) + i 0.4940(2)	-1.4799 + i 0.4977
$++00$	17.2585(6) + i 29.5669(6)	17.2602 + i 29.5643
$+-00$	10.2869(5) - i 1.0571(6)	10.2840 - i 1.0640

Table 2. Comparison of the NLO helicity amplitudes between the exact numerical values and the values given by the p_T expansion at $\mathcal{O}(p_T^4)$ in the kinematic point provided in ref. [43].

`Mathematica` and `FeynCalc`. The amplitude was contracted with the 18 projectors in appendix A and each form factor expanded up to $\mathcal{O}(p_T^4)$. This led to the identification of a set of 9 families of scalar integrals. These families were analyzed using `LiteRed` and reduced to a basis of 52 known MIs [33, 34, 57–60], which we found to be the same as those encoutered in HH and ZH production. Among the 52 MI, fifty can be expressed in terms of (generalised) harmonic polylogarithms while two are elliptic integrals. The evaluation of the (generalised) harmonic polylogarithms was done using the code `handyG` [61], while the elliptic integrals were evaluated using the routines of ref. [62]. The top quark mass was renormalised in the on-shell scheme and the infra-red (IR) poles were subtracted[5] as in refs. [63, 64].

As a first check of our computation, we compared our p_T-expanded result with the LME one presented in ref. [42]. It should be noticed that the p_T-expanded result actually "contains" the LME one. The LME differs from the expansion in p_T by the fact that $\hat{s}$ is treated as a small parameter with respect to m_t^2, and not on the same footing as in the latter case. This implies that when the p_T-expanded result is further expanded in terms of the $\hat{s}/m_t^2$ ratio the LME result has to be recovered. This way, we were able to reproduce, at the analytic level, the LME result of ref. [42] up to the order of our calculation.

As a second check of our computation we compare, in table 2, the contribution of the two-loop box diagrams at $\mathcal{O}(p_T^4)$ with the results of ref. [43], which rely on the numerical evaluation of the scalar integrals. The comparison is done at the level of the helicity amplitudes[6] for the fixed phase-space point presented in ref. [43], defined as $\hat{s} = 142/17\ m_t^2$ and $\hat{t} = -125/22\ m_t^2 \sim -5.7\ m_t^2$. We remark that the IR subtraction scheme employed in ref. [43] (q_T subtraction) differs from ours, so that to reproduce the form factors of ref. [43], $\mathcal{A}_i^{(1)q_T}$, a shift in our form factors has to be introduced as follows:

$$\mathcal{A}_i^{(1)q_T} = \mathcal{A}_i^{(1)} + \frac{C_A}{4}\pi^2\,. \tag{4.1}$$

We notice that although the point chosen in ref. [43] has $|\hat{t}| > 4m_t^2$, the value of $\hat{s}$ is still

[5] In the calculation we employed the background field method that allows to separate the renormalization of α_s from the rest of the computation. Then, our IR subtraction does not take into account the renormalization of α_s whose contribution to the amplitude is well known.

[6] The helicities of the polarization vectors are defined as: $\epsilon_\mu^{\lambda_1}(p_1)\,\epsilon_\nu^{\lambda_2}(p_2)\,\epsilon_\rho^{*\,\lambda_3}(p_3)\,\epsilon_\sigma^{*\,\lambda_4}(p_4)$.

JHEP07(2024)244

sufficiently low that this point can be covered by the p_T expansion. In particular $|\hat{u}| < 4m_t^2$, and in this case a *backward* expansion can be obtained from the *forward* one by symmetry (see also the discusison in ref. [48]). Indeed, table 2 shows that the relative difference between the $\mathcal{O}(p_T^4)$ values and the numerical ones is, in general with the exception of only one helicity amplitude, at the per mille level and often better, as in the case of the amplitudes involving two longitudinally-polarized Z bosons. The latter amplitudes are the dominant ones, as consequence of the Goldstone Boson Equivalence Theorem.

4.2 Merging the p_T and high-energy expansions

The results we have presented so far allow to efficiently approximate the two-loop box integrals with full top-mass dependence over a specific region of the phase space, which spans the ZZ production threshold up to moderate partonic centre-of-mass energies (for the LHC). In the high-energy region the p_T expansion is still accurate for any values of $\hat{s}$ and $|\hat{t}| \lesssim 4m_t^2$ or $|\hat{u}| \lesssim 4m_t^2$ but it cannot cover the complementary region $|\hat{t}|, |\hat{u}| \gtrsim 4m_t^2$ that becomes allowed by the kinematics.

In ref. [48] we showed that the p_T expansion and the HE expansion are accurate in complementary phase-space regions. The HE expansion is an expansion in terms of the ratios x/y where $x \in \{m_t^2, m_Z^2\}$ and $y \in \{\hat{s}, \hat{t}, \hat{u}\}$ and it is valid in phase-space regions where both $|\hat{t}|/(4\,m_t^2) \gtrsim 1$ and $|\hat{u}|/(4\,m_t^2) \gtrsim 1$. We also showed that if each expansion is extended beyond its border of validity via the use of Padé approximants the two results can be merged into a single prediction that is accurate over the complete phase space.

Results for the evaluation of the two-loop box contribution in the $gg \to ZZ$ process via the HE expansion were presented in ref. [42]. Applying the method of ref. [48] we merge our results for the box contribution with those obtained in ref. [42]. Below we recall the main steps of the merging method:

1. We use the formulas in eqs. (A.21)–(A.38) to adapt the form factors of ref. [42] to our decomposition of the amplitude.

2. We rewrite the small quantities on which the p_T and the HE expansions are based in terms of a scaling parameter x.

3. We construct Padé approximants for each form factor, defined as

$$[m/n](x) = \frac{p_0 + p_1 x + \cdots + p_m x^m}{1 + q_1 x + \ldots q_n x^n}, \tag{4.2}$$

   where p_i, q_i are expressed as linear combinations of the coefficients of each expansion. We refer to these approximants as the p_T-Padé and HE-Padé.

4. In evaluating the amplitude, we use the HE-Padé approximant for phase-space points such that $|\hat{t}| > 4m_t^2$ and $|\hat{u}| > 4m_t^2$ whereas for all the remaining phase-space points we use the p_T-Padé approximant.

With our three terms in the p_T expansion we constructed a [1/1] p_T-Padé. The several terms in the HE expansion presented in ref. [42] allow to construct different [x/y] HE-Padé. We construct both the [5/5] and [6/6] HE-Padé and compare the results using the different orders. As a result we found that both the [5/5] and [6/6] HE-Padé give very similar results.

JHEP07(2024)244

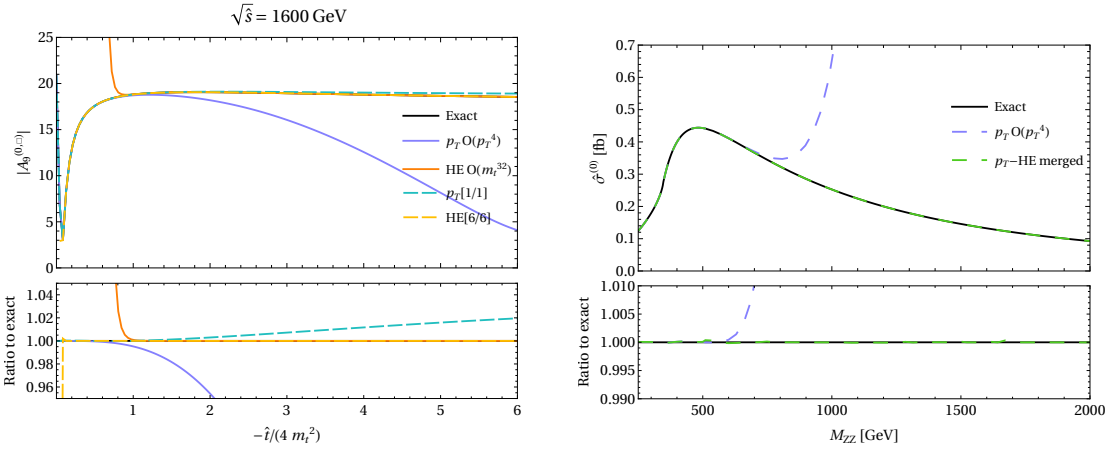

(a) (b)

Figure 4. (a) Absolute value of a form factor for a fixed $\sqrt{\hat{s}}$ using the p_T and the HE expansion and the best Padé approximants. (b) Partonic cross section at LO using the exact result, the p_T expansion and the prediction using the merged p_T and HE Padé approximants.

5 Results

Before applying the merging approach for the form factors at NLO, we verified its reliability testing it against the exact LO contribution. In figure 4(a) the exact result (solid black line) for the form factor, $\mathcal{A}_9^{(0,\square)}$ as a function of $-\hat{t}/(4\,m_t^2)$ is compared to different approximate evaluations. In the figure the fixed order results $\mathcal{O}(p_T^4)$ in the p_T expansion (solid blue) and $\mathcal{O}(m_t^{32})$ in the HE expansion (solid orange) are shown against the Padé-improved versions, [1/1] p_T-Padé (dashed light blue) and [6/6] HE-Padé (dashed yellow). The bottom panel shows the ratio of the different approximations over the exact result. It is evident that the region $|\hat{t}| \sim 4\,m_t^2$, where both the p_T and HE expansions (solid blue and orange) begin to diverge, is well covered by the respective Padé approximants, so that one has a way to accurately reproduce the exact result for any value of $|\hat{t}|$. In figure 4(b) we compare different predictions at the level of the LO partonic cross section. One can see that the accuracy of the merged result (dashed green) is at the level of per mille or below, an order of magnitude better than what observed in ref. [48]. We notice that, this remarkable degree of accuracy is not achieved for each individual form factor. However, the impact of larger deviations is suppressed with the integration over $\hat{t}$.

We now present our results at NLO. First, we checked their the validity in two ways:

- We compared the p_T-Padé and HE-Padé in the vicinity of $|\hat{t}| \sim 4m_t^2$, for several values of $\hat{s}$ in the range [800, 2000] GeV, ensuring that the two analytic approximations are indeed complementary and that the matching point is chosen well. In figure 5 the NLO form factor $\mathcal{A}_9^{(1,\square)}$ is shown as a function of $-\hat{t}/(4\,m_t^2)$ for both fixed-order p_T and HE expansions and Padé-improved results. The lower panel of the figure shows the relative difference, Δ, between the p_T-Padé and the HE-Padé, defined as

$$\Delta = 2\left|\frac{[1/1]_{p_T} - [6/6]_{\mathrm{HE}}}{[1/1]_{p_T} + [6/6]_{\mathrm{HE}}}\right|, \tag{5.1}$$

  where one can see that at $|\hat{t}| \sim 4m_t^2$ the two expansion are in good agreement (on the level of 0.5 per mille).

JHEP07(2024)244

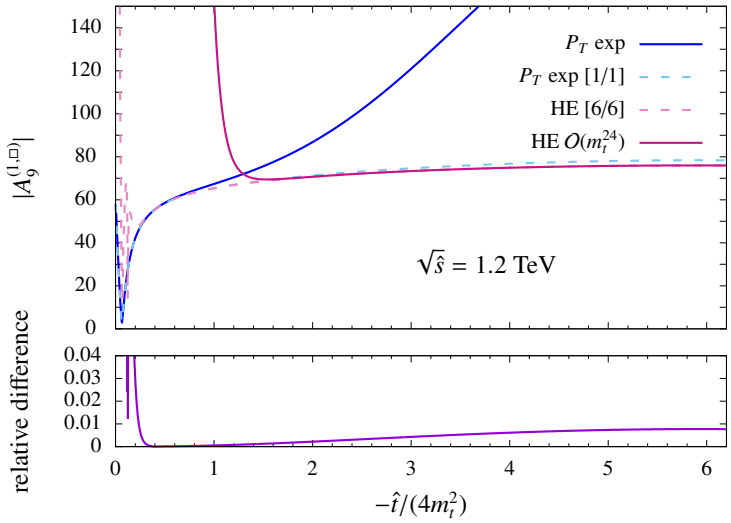

Figure 5. NLO form factor for $\sqrt{\hat{s}} = 1200$ GeV in various approximations: p_T expansion (solid blue), [1/1] Padé approximant based on the p_T expansion (dashed, light blue), high-energy expansion (solid, pink) and [6/6] HE Padé approximant (dashed, rosa). The lower panel shows the relative difference Δ (see text).

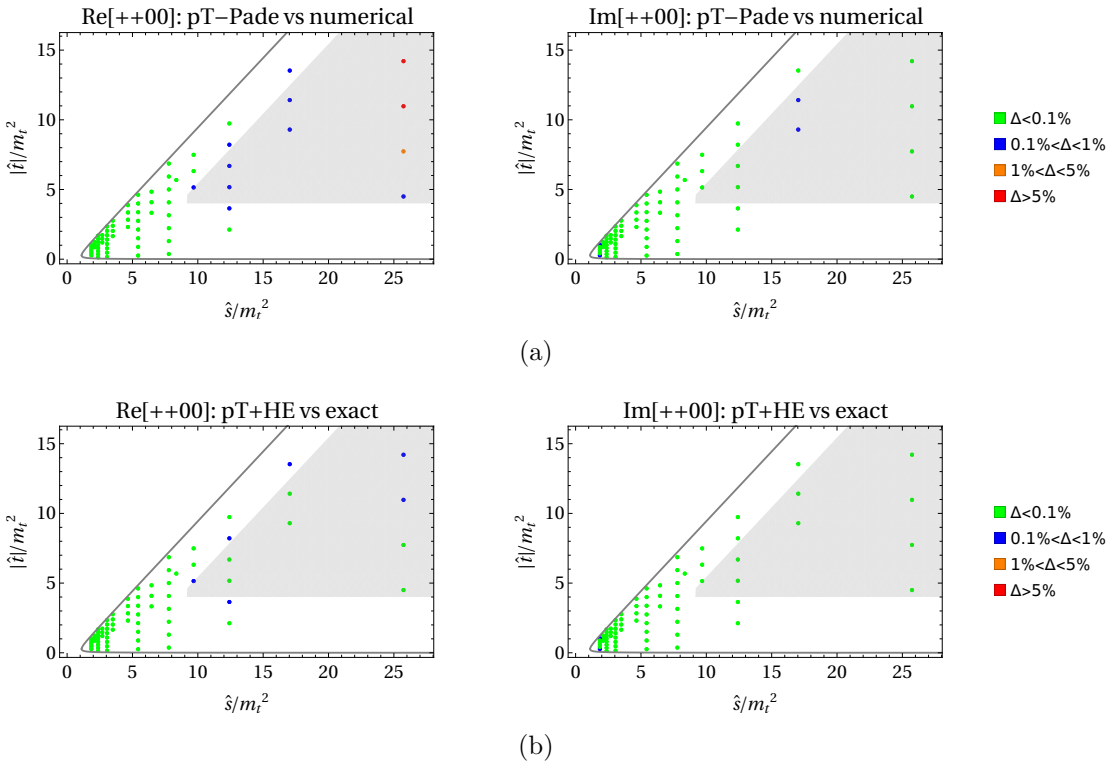

Figure 6. Relative difference between several phase-space points of ref. [43] and different approximations for the helicity amplitude ++00. Points in the shaded region are outside the formal limit of validity of the p_T expansion. The physical phase-space region is delimited by the grey line. (a) [1/1] p_T-Padé only; (b) merging of the p_T-Padé and the HE-Padé.

JHEP07(2024)244

- We compared our merged results with the helicity amplitudes of ref. [43], obtained from a numerical evaluation of the scalar integrals. The results for several phase-space points were provided privately by the authors of ref. [43]. In figure 6 we plot the results for the amplitude $++00$ using different colors depending on the level of agreement Δ between the numerical and merged prediction. The shaded region in the plots corresponds to the high-energy region, where $|\hat{t}| > 4m_t^2$ and $|\hat{u}| > 4m_t^2$. In figure 6 (a) we compare the numerical evaluation with our results using only the [1/1] p_T-Padé. Whereas the agreement is generally better than per mille in the region of validity of the p_T expansion, deviations larger than 5% are visible in the high-energy region for the real part. When we consider the merged prediction, the agreement with the numerical evaluation is improved, and the majority of the phase space points have differences below the per mille level. For the blue points at large and small values of $\hat{s}/m_t^2$ in figure 6 (b) the deviations are within the error of the numerical result. The other blue points are located at the border of validity of both expansions, and for some of them the deviations are outside the numerical error. However, in this case we expect that the accuracy of the Padé approximants cannot be as good as for the other regions. It must be noted that, as seen in table 2, the above level of agreement is not shared among all the helicity amplitudes. This is however a consequence of the relations used to convert our results in terms of form factors into helicity amplitudes. Indeed, for some phase-space points, we observed delicate cancellations in the combination of the form factors. At the same time, for these particular phase-space points, the corresponding contributions to the helicity amplitudes are tiny. Therefore, we expect an overall accuarcy at the subpercent level for our results.

In figure 7 one can see our result for the finite part of the virtual corrections defined as

$$\Delta\sigma_{\text{virt}} = \int_{\hat{t}^-}^{\hat{t}^+} d\hat{t} \frac{1}{2} \frac{1}{16\pi\hat{s}^2} \left(\frac{\alpha_s(\mu_R)}{\pi}\right) \mathcal{V}_{\text{fin}}(\hat{t}) \tag{5.2}$$

where the finite part of the virtual correction is

$$\mathcal{V}_{\text{fin}} = \frac{G_F^2 m_Z^4}{16} \left(\frac{\alpha_s(\mu_R)}{\pi}\right)^2 \left\{ \sum_i \left|\mathcal{A}_i^{(0)}\right|^2 \frac{C_A}{2} \left(\pi^2 - \log^2\left(\frac{\mu_R^2}{\hat{s}}\right)\right) + 2 \sum_i \text{Re}\left[\mathcal{A}_i^{(0)} \left(\mathcal{A}_i^{(1)}\right)^*\right] \right\}. \tag{5.3}$$

We used $\mu_R = M_{ZZ}/2$ as renormalisation scale. The pink line shows the merged result of a [1/1] p_T-expanded Padé approximant and a [6/6] HE Padé approximant. For comparison we show the large mass expanded results of ref. [42]. Within the range of validity of the large mass expansion the results agree very well. We have checked that using a [5/5] HE Padé approximant would change the result only below the integration error.

6 Conclusion

The accurate description of the process $gg \to ZZ$ is needed in order to improve the extraction of the total width of the Higgs boson, as well as a precision test for the SM. In this paper we have presented the calculation of the top-quark loops in the virtual QCD corrections at NLO. Our main result is the computation of the box diagrams using the p_T expansion,

JHEP07(2024)244

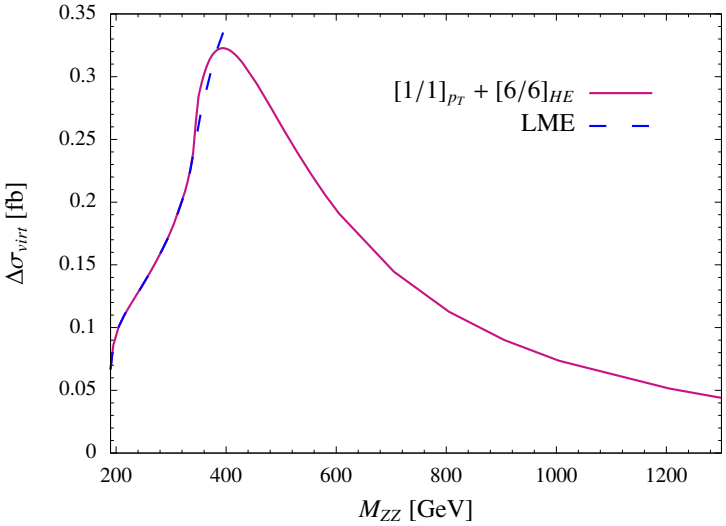

Figure 7. The partonic virtual corrections as a function of M_{zz} merging the p_T and the HE expansions (pink solid line) compared to the virtual corrections obtained when using the large mass expanded results for the NLO box and triangles (dashed blue line).

which gives accurate results in a phase-space region that so far has not been covered by other analytic approximations.

As a by-product of our calculation, we have used the results obtained in ref. [42] to complement our analytic calculation, showing that a combination of the two approaches can provide an efficient approximation for the cross section, at a level of accuracy that is more than adequate for phenomenological applications. We emphasise that our analytic approach is very flexible and can be included into Monte Carlo programmes, as was already done for the case of Higgs pair production, $gg \to HH$ [65]. It allows to change easily the input parameters, which is for instance necessary to evaluate the top-mass renormalisation scheme uncertainty that is expected to be large in the top-mediated contributions. Indeed, it is currently the largest uncertainty for the $gg \to HH$ [66, 67] and $gg \to ZH$ [68] processes. In addition, the flexibility of the approach allows for a straightforward application to beyond-the-SM scenarios.

We recall that for a full description of $gg \to ZZ$ at NLO in QCD also the contribution mediated by loops of light quarks needs to be considered [36, 37], as well as the one from real-emission diagrams [17]. We leave the combination of these effects with our results to future work.

Acknowledgments

We thank Luigi Bellafronte and Pier Paolo Giardino for participating in the early stages of this project. We are greatful to the authors of ref. [43] for providing us with the results for additional phase-space points and for useful discussions. The work of RG is supported in part by the Italian MUR Departments of Excellence grant 2023-2027 "Quantum Frontiers" and the ICSC — Centro Nazionale di Ricerca in High Performance Computing, Big Data and Quantum Computing, funded by European Union — NextGenerationEU. The authors acknowledge support from the COMETA COST Action CA22130. The diagrams in this paper have been drawn using `JaxoDraw` [69].

JHEP07(2024)244

A Projectors

We present the explicit expressions of the orthonormal projectors $\mathcal{P}_i^{\mu\nu\rho\sigma}$ appearing in eq. (2.7). Following the notation of section 2, the antisymmetric projectors under the exchange $\{\mu \leftrightarrow \nu,\ p_1 \leftrightarrow p_2\}$ are

$$\mathcal{P}_1^{\mu\nu\rho\sigma} = \frac{m_Z}{\sqrt{2}p_T}\left[\frac{1}{p_T^2 s'}\left(S_{17}^{\mu\nu\rho\sigma} - S_{20}^{\mu\nu\rho\sigma}\right)\right] \tag{A.1}$$

$$\mathcal{P}_2^{\mu\nu\rho\sigma} = \frac{m_Z}{\sqrt{2}p_T}\left[\frac{1}{p_T^2 s'}\left(\frac{t'}{u'}S_{19}^{\mu\nu\rho\sigma} - \frac{u'}{t'}S_{18}^{\mu\nu\rho\sigma}\right)\right] \tag{A.2}$$

$$\mathcal{P}_3^{\mu\nu\rho\sigma} = \frac{m_Z}{\sqrt{2}p_T}\left[\frac{S_5^{\mu\nu\rho\sigma}}{u'} - \frac{S_6^{\mu\nu\rho\sigma}}{t'} - \frac{1}{p_T^2 s'}\left(S_{17}^{\mu\nu\rho\sigma} - S_{20}^{\mu\nu\rho\sigma} + \frac{u'}{t'}S_{18}^{\mu\nu\rho\sigma} - \frac{t'}{u'}S_{19}^{\mu\nu\rho\sigma}\right)\right] \tag{A.3}$$

$$\mathcal{P}_4^{\mu\nu\rho\sigma} = \frac{m_Z}{\sqrt{2}p_T}\left[\frac{1}{s'}\left(S_9^{\mu\nu\rho\sigma} - S_{12}^{\mu\nu\rho\sigma}\right) + \frac{1}{p_T^2 s'}\left(S_{17}^{\mu\nu\rho\sigma} - S_{20}^{\mu\nu\rho\sigma}\right)\right] \tag{A.4}$$

$$\mathcal{P}_5^{\mu\nu\rho\sigma} = \frac{m_Z}{\sqrt{2}p_T}\left[\frac{1}{s'}\left(\frac{t'}{u'}S_{11}^{\mu\nu\rho\sigma} - \frac{u'}{t'}S_{10}^{\mu\nu\rho\sigma}\right) + \frac{1}{p_T^2 s'}\left(\frac{t'}{u'}S_{19}^{\mu\nu\rho\sigma} - \frac{u'}{t'}S_{18}^{\mu\nu\rho\sigma}\right)\right] \tag{A.5}$$

$$\mathcal{P}_6^{\mu\nu\rho\sigma} = \frac{m_Z}{\sqrt{2}p_T}\left[\frac{S_{13}^{\mu\nu\rho\sigma}}{u'} - \frac{S_{16}^{\mu\nu\rho\sigma}}{t'} - \frac{1}{p_T^2 s'}\left(S_{17}^{\mu\nu\rho\sigma} - S_{20}^{\mu\nu\rho\sigma} + \frac{t'}{u'}S_{19}^{\mu\nu\rho\sigma} - \frac{u'}{t'}S_{18}^{\mu\nu\rho\sigma}\right)\right] \tag{A.6}$$

$$\begin{aligned}\mathcal{P}_7^{\mu\nu\rho\sigma} = \frac{m_Z^2}{\sqrt{2}p_T^2}\Bigg[&\frac{(m_Z^2 - p_T^2)}{2m_Z^2}\left(\frac{S_{13}^{\mu\nu\rho\sigma}}{u'} - \frac{S_{16}^{\mu\nu\rho\sigma}}{t'}\right) + \frac{1}{m_Z^2 s'}\left(u' S_{14}^{\mu\nu\rho\sigma} - t' S_{15}^{\mu\nu\rho\sigma}\right) \\ &+ \frac{1}{m_Z^2 s'}\left(S_{17}^{\mu\nu\rho\sigma} - S_{20}^{\mu\nu\rho\sigma} + \frac{t'}{u'}S_{19}^{\mu\nu\rho\sigma} - \frac{u'}{t'}S_{18}^{\mu\nu\rho\sigma}\right)\Bigg]\end{aligned} \tag{A.7}$$

$$\begin{aligned}\mathcal{P}_8^{\mu\nu\rho\sigma} = \frac{m_Z^2}{\sqrt{2}p_T^2}\Bigg[&\frac{1}{m_Z^2 s'}\left(u' S_4^{\mu\nu\rho\sigma} - t' S_7^{\mu\nu\rho\sigma}\right) + \frac{(m_Z^2 - p_T^2)}{2m_Z^2}\left(\frac{S_5^{\mu\nu\rho\sigma}}{u'} - \frac{S_6^{\mu\nu\rho\sigma}}{t'}\right) \\ &+ \frac{1}{m_Z^2 s'}\left(S_{17}^{\mu\nu\rho\sigma} - S_{20}^{\mu\nu\rho\sigma} + \frac{u'}{t'}S_{18}^{\mu\nu\rho\sigma} - \frac{t'}{u'}S_{19}^{\mu\nu\rho\sigma}\right)\Bigg].\end{aligned} \tag{A.8}$$

The symmetric projectors are

$$\mathcal{P}_9^{\mu\nu\rho\sigma} = \frac{m_Z^2}{\sqrt{p_T^4 + m_Z^4}}\left[\frac{1}{p_T^2 s'}\left(S_{17}^{\mu\nu\rho\sigma} + S_{20}^{\mu\nu\rho\sigma}\right)\right] \tag{A.9}$$

$$\mathcal{P}_{10}^{\mu\nu\rho\sigma} = \frac{\sqrt{p_T^4 + m_Z^4}}{2p_T^2}\left[\frac{(m_Z^4 - p_T^4)}{(m_Z^4 + p_T^4)\,p_T^2 s'}\left(S_{17}^{\mu\nu\rho\sigma} + S_{20}^{\mu\nu\rho\sigma}\right) + \frac{1}{p_T^2 s'}\left(\frac{u'}{t'}S_{18}^{\mu\nu\rho\sigma} + \frac{t'}{u'}S_{19}^{\mu\nu\rho\sigma}\right)\right] \tag{A.10}$$

$$\mathcal{P}_{11}^{\mu\nu\rho\sigma} = \frac{m_Z^2}{\sqrt{p_T^4 + m_Z^4}}\left[\frac{1}{s'}\left(S_9^{\mu\nu\rho\sigma} + S_{12}^{\mu\nu\rho\sigma}\right) + \frac{1}{p_T^2 s'}\left(S_{17}^{\mu\nu\rho\sigma} + S_{20}^{\mu\nu\rho\sigma}\right)\right] \tag{A.11}$$

$$\begin{aligned}\mathcal{P}_{12}^{\mu\nu\rho\sigma} = \frac{\sqrt{p_T^4 + m_Z^4}}{2p_T^2}\Bigg[&\frac{(m_Z^4 - p_T^4)}{(m_Z^4 + p_T^4)\,s'}\left(S_9^{\mu\nu\rho\sigma} + S_{12}^{\mu\nu\rho\sigma}\right) + \frac{1}{s'}\left(\frac{u'}{t'}S_{10}^{\mu\nu\rho\sigma} + \frac{t'}{u'}S_{11}^{\mu\nu\rho\sigma}\right) \\ &+ \frac{(m_Z^4 - p_T^4)}{(m_Z^4 + p_T^4)\,p_T^2 s'}\left(S_{17}^{\mu\nu\rho\sigma} + S_{20}^{\mu\nu\rho\sigma}\right) + \frac{1}{p_T^2 s'}\left(\frac{u'}{t'}S_{18}^{\mu\nu\rho\sigma} + \frac{t'}{u'}S_{19}^{\mu\nu\rho\sigma}\right)\Bigg]\end{aligned} \tag{A.12}$$

JHEP07(2024)244

$$\mathcal{P}_{13}^{\mu\nu\rho\sigma} = \frac{m_Z}{\sqrt{2}p_T}\left[\frac{S_{13}^{\mu\nu\rho\sigma}}{u'}+\frac{S_{16}^{\mu\nu\rho\sigma}}{t'}-\frac{1}{p_T^2 s'}\left(S_{17}^{\mu\nu\rho\sigma}+S_{20}^{\mu\nu\rho\sigma}\right)-\frac{1}{p_T^2 s'}\left(\frac{u'}{t'}S_{18}^{\mu\nu\rho\sigma}+\frac{t'}{u'}S_{19}^{\mu\nu\rho\sigma}\right)\right] \tag{A.13}$$

$$\begin{aligned}\mathcal{P}_{14}^{\mu\nu\rho\sigma} = \frac{m_Z^2}{\sqrt{2}p_T^2}\Bigg[&\frac{\left(m_Z^2-p_T^2\right)}{2m_Z^2}\left(\frac{S_{13}^{\mu\nu\rho\sigma}}{u'}+\frac{S_{16}^{\mu\nu\rho\sigma}}{t'}\right)+\frac{1}{m_Z^2 s'}\left(u'S_{14}^{\mu\nu\rho\sigma}+t'S_{15}^{\mu\nu\rho\sigma}\right)\\ &-\frac{1}{p_T^2 s'}\left(S_{17}^{\mu\nu\rho\sigma}+S_{20}^{\mu\nu\rho\sigma}+\frac{u'}{t'}S_{18}^{\mu\nu\rho\sigma}+\frac{t'}{u'}S_{19}^{\mu\nu\rho\sigma}\right)\Bigg]\end{aligned} \tag{A.14}$$

$$\begin{aligned}\mathcal{P}_{15}^{\mu\nu\rho\sigma} = \frac{\sqrt{2}m_Z^3}{p_T\left(p_T^2+m_Z^2\right)}\Bigg[&\frac{1}{m_Z^2 s'}\left(u'S_4^{\mu\nu\rho\sigma}+t'S_7^{\mu\nu\rho\sigma}\right)\\ &+\frac{\left(m_Z^2+p_T^2\right)}{2m_Z^2 p_T^2 s'}\left(S_{17}^{\mu\nu\rho\sigma}+S_{20}^{\mu\nu\rho\sigma}+\frac{u'}{t'}S_{18}^{\mu\nu\rho\sigma}+\frac{t'}{u'}S_{19}^{\mu\nu\rho\sigma}\right)\Bigg]\end{aligned} \tag{A.15}$$

$$\begin{aligned}\mathcal{P}_{16}^{\mu\nu\rho\sigma} = \frac{p_T^2+m_Z^2}{2\sqrt{2}p_T^2}\Bigg[&\frac{2m_Z^2}{s'p_T^2\left(p_T^2+m_Z^2\right)}\left(S_{17}^{\mu\nu\rho\sigma}+S_{20}^{\mu\nu\rho\sigma}+\frac{u'}{t'}S_{18}^{\mu\nu\rho\sigma}+\frac{t'}{u'}S_{19}^{\mu\nu\rho\sigma}\right)\\ &-\frac{2\left(p_T^2-m_Z^2\right)}{\left(m_Z^2+p_T^2\right)^2 s'}\left(u'S_4^{\mu\nu\rho\sigma}+t'S_7^{\mu\nu\rho\sigma}\right)+\frac{S_5^{\mu\nu\rho\sigma}}{u'}+\frac{S_6^{\mu\nu\rho\sigma}}{t'}\Bigg]\end{aligned} \tag{A.16}$$

$$\begin{aligned}\mathcal{P}_{17}^{\mu\nu\rho\sigma} = \frac{p_T^2+2m_Z^2}{2m_Z^2}\Bigg\{&\frac{m_Z^2}{2m_Z^2+p_T^2}\left(S_2^{\mu\nu\rho\sigma}+S_3^{\mu\nu\rho\sigma}\right)-\frac{m_Z^2}{\left(p_T^2+2m_Z^2\right)s'p_T^2}\left(u'S_4^{\mu\nu\rho\sigma}+t'S_7^{\mu\nu\rho\sigma}\right)\\ &-\frac{\left(m_Z^2+p_T^2\right)m_Z^2}{p_T^2\left(2m_Z^2+p_T^2\right)}\Bigg[\frac{S_5^{\mu\nu\rho\sigma}}{2u'}+\frac{S_6^{\mu\nu\rho\sigma}}{2t'}-\frac{S_{13}^{\mu\nu\rho\sigma}}{2u'}-\frac{S_{16}^{\mu\nu\rho\sigma}}{2t'}+\frac{1}{p_T^2 s'}\Bigg(S_{17}^{\mu\nu\rho\sigma}+S_{20}^{\mu\nu\rho\sigma}\\ &+\frac{u'}{t'}S_{18}^{\mu\nu\rho\sigma}+\frac{t'}{u'}S_{19}^{\mu\nu\rho\sigma}\Bigg)\Bigg]+\frac{m_Z^2}{p_T^2 s'\left(2m_Z^2+p_T^2\right)}\left(u'S_{14}^{\mu\nu\rho\sigma}+t'S_{15}^{\mu\nu\rho\sigma}\right)\Bigg\}\end{aligned} \tag{A.17}$$

$$\begin{aligned}\mathcal{P}_{18}^{\mu\nu\rho\sigma} = &\frac{S_8^{\mu\nu\rho\sigma}}{p_T^2}-\frac{\left(m_Z^2+p_T^2\right)}{2p_T^4 s'}\left(S_{17}^{\mu\nu\rho\sigma}+S_{20}^{\mu\nu\rho\sigma}\right)+\frac{u'\ \left(-m_Z^4+p_T^4-2p_T^2(s'-t'+u')\right)S_{18}^{\mu\nu\rho\sigma}}{2p_T^4\ \left(m_Z^2+p_T^2\right)s't'}\\ &-\frac{t'\ \left(m_Z^4-p_T^4+2p_T^2(s'+t'-u')\right)S_{19}^{\mu\nu\rho\sigma}}{2p_T^4\ \left(m_Z^2+p_T^2\right)s'\ u'}.\end{aligned} \tag{A.18}$$

Finally, we include the last two projectors, which have null norm in $D=4$ dimensions and thus do not contribute to the amplitude.

$$\begin{aligned}\mathcal{P}_{19}^{\mu\nu\rho\sigma} = &S_1^{\mu\nu\rho\sigma}-\frac{S_2^{\mu\nu\rho\sigma}}{2}-\frac{S_3^{\mu\nu\rho\sigma}}{2}+\frac{1}{2\ p_T^2 s'}\left(u'S_4^{\mu\nu\rho\sigma}+t'S_7^{\mu\nu\rho\sigma}\right)+\frac{\left(m_Z^2+p_T^2\right)}{4\ p_T^2}\left(\frac{S_5^{\mu\nu\rho\sigma}}{u'}+\frac{S_6^{\mu\nu\rho\sigma}}{t'}\right)\\ &+\frac{S_8^{\mu\nu\rho\sigma}}{p_T^2}-\frac{\left(m_Z^2+p_T^2\right)}{2p_T^2 s'}\left(S_9^{\mu\nu\rho\sigma}+S_{12}^{\mu\nu\rho\sigma}\right)+\frac{u'\ \left(-m_Z^4+p_T^4-2p_T^2(s'-t'+u')\right)S_{10}^{\mu\nu\rho\sigma}}{2p_T^2\ \left(m_Z^2+p_T^2\right)s't'}\\ &-\frac{t'\ \left(m_Z^4-p_T^4+2p_T^2(s'+t'-u')\right)S_{11}^{\mu\nu\rho\sigma}}{2p_T^2\ \left(m_Z^2+p_T^2\right)s'\ u'}-\frac{\left(m_Z^2+p_T^2\right)}{4p_T^2}\left(\frac{S_{13}^{\mu\nu\rho\sigma}}{u'}+\frac{S_{16}^{\mu\nu\rho\sigma}}{t'}\right)\\ &-\frac{1}{2p_T^2 s'}\left(u'S_{14}^{\mu\nu\rho\sigma}+t'\ S_{15}^{\mu\nu\rho\sigma}\right)+\frac{\left(m_Z^2+p_T^2-s'+t'-u'\right)u'S_{18}^{\mu\nu\rho\sigma}}{p_T^2\left(m_Z^2+p_T^2\right)\ s't'}\\ &+\frac{t'\ \left(m_Z^2+p_T^2-s'-t'+u'\right)\ S_{19}^{\mu\nu\rho\sigma}}{p_T^2\left(m_Z^2+p_T^2\right)s'\ u'}\end{aligned} \tag{A.19}$$

$$\mathcal{P}_{20}^{\mu\nu\rho\sigma} = \frac{1}{2m_Z^2+p_T^2}\Bigg[S_3^{\mu\nu\rho\sigma} - S_2^{\mu\nu\rho\sigma} - \frac{1}{p_T^2 s'}\left(u' S_4^{\mu\nu\rho\sigma} - t' S_7^{\mu\nu\rho\sigma} + u' S_{14}^{\mu\nu\rho\sigma} - t' S_{15}^{\mu\nu\rho\sigma}\right) \tag{A.20}$$
$$- \frac{(m_Z^2+p_T^2)}{2p_T^2}\left(\frac{S_5^{\mu\nu\rho\sigma}}{u'} - \frac{S_6^{\mu\nu\rho\sigma}}{t'} + \frac{S_{13}^{\mu\nu\rho\sigma}}{u'} - \frac{S_{16}^{\mu\nu\rho\sigma}}{t'}\right)\Bigg]$$

The form factors $\mathcal{A}_i$ associated to the above projectors can be expressed in terms of the form factors f_i defined in eq. (2.8) of ref. [42] via the following relations

$$\mathcal{A}_1 = 0 \tag{A.21}$$

$$\mathcal{A}_2 = \frac{p_T^2}{m_Z^2}\Bigg[\frac{2(t'-u')}{(m_Z^2+p_T^2)}\left(p_T^2 f_8 - f_1\right) + s' p_T^2\left(\frac{u'}{t'} f_{19} - \frac{t'}{u'} f_{18}\right) \tag{A.22}$$
$$+ 2t' f_4 - 2u' f_5 + 2t' f_6 - 2u' f_7 + \frac{s't'}{u'} f_{10} - \frac{s'u'}{t'} f_{11}\Bigg]$$

$$\mathcal{A}_3 = \frac{p_T^2}{m_Z^2}\left[f_3 - f_2 + \frac{(m_Z^2-p_T^2)\,s'}{2}\left(\frac{f_7}{t'} - \frac{f_4}{u'}\right) + u' f_5 - t' f_6\right] \tag{A.23}$$

$$\mathcal{A}_4 = 0 \tag{A.24}$$

$$\mathcal{A}_5 = \frac{p_T^2}{m_Z^2}\left[\frac{2(t'-u')}{(m_Z^2+p_T^2)} f_1 + \frac{s'u'}{t'} f_{11} - \frac{s't'}{u'} f_{10}\right] \tag{A.25}$$

$$\mathcal{A}_6 = \frac{p_T^2}{m_Z^2}\left[f_3 - f_2 + t' f_4 - u' f_7 + \frac{(m_Z^2-p_T^2)\,s'}{2}\left(\frac{f_6}{u'} - \frac{f_5}{u'}\right)\right] \tag{A.26}$$

$$\mathcal{A}_7 = \frac{p_T^2}{m_Z^2}\left[f_3 - f_2 + \frac{\left(3s'm_Z^2 + p_T^2 s' - 2\left(u'm_Z^2 + t'\left(m_Z^2+u'\right)\right)\right)p_T^2}{4m_Z^2}\left(\frac{f_5}{t'} - \frac{f_6}{u'}\right)\right] \tag{A.27}$$

$$\mathcal{A}_8 = \frac{p_T^2}{m_Z^2}\left[f_3 - f_2\frac{\left(3s'm_Z^2 + p_T^2 s' - 2\left(u'm_Z^2 + t'\left(m_Z^2+u'\right)\right)\right)p_T^2}{4m_Z^2}\left(\frac{f_4}{u'} - \frac{f_7}{t'}\right)\right] \tag{A.28}$$

$$\mathcal{A}_9 = \frac{1}{m_Z^4}\Bigg[-2p_T^4\left(t' f_4 + u' f_5 + t' f_6 + u' f_7\right) - \left(m_Z^2+p_T^2\right)p_T^2\left(f_2+f_3\right) \tag{A.29}$$
$$- \frac{\left(s'(m_Z^2+p_T^2)(m_Z^2-s') + 2m_Z^2(t'^2+u'^2)\right)}{s'}\left(p_T^2 f_8 - f_1\right) - s'\left(m_Z^4+p_T^4\right)\left(f_9 - p_T^2 f_{20}\right)$$
$$+ \frac{2\left(u'm_Z^2 + t'\left(m_Z^2+u'\right)\right)}{s'}\left(p_T^2\left(t'^2 f_{18} + u'^2 f_{19}\right) - \left(t'^2 f_{10} + u'^2 f_{11}\right)\right)\Bigg]$$

$$\mathcal{A}_{10} = \frac{2p_T^2}{(m_Z^4+p_T^4)}\Bigg[s' p_T^2\left(p_T^2\left(\frac{t'}{u'} f_{18} + \frac{u'}{t'} f_{19}\right) - \left(\frac{t'}{u'} f_{10} + \frac{u'}{t'} f_{11}\right)\right) - 2p_T^2\left(t' f_4 + u' f_5 + t' f_6 + u' f_7\right)$$
$$+ \frac{\left(\left(s'^2 - t'^2 - u'^2\right)m_Z^2 + p_T^2\left(s'^2 + t'^2 + u'^2\right)\right)}{\left(m_Z^2+p_T^2\right)s'}\left(f_8 p_T^2 - f_1\right) - \left(m_Z^2+p_T^2\right)\left(f_2+f_3\right)\Bigg] \tag{A.30}$$

$$\mathcal{A}_{11} = \frac{1}{m_Z^4}\Bigg[s'\left(m_Z^4+p_T^4\right) f_9 + \frac{2\left(u'm_Z^2 + t'\left(m_Z^2+u'\right)\right)}{s'}\left(t'^2 f_{10} + u'^2 f_{11}\right) \tag{A.31}$$
$$- \frac{\left(2u'^2 m_Z^2 + s'\left(m_Z^2+u'\right)\left(s'm_Z^2 + 2t'^2 + p_T^2 s'\right)\right)}{s'} f_1\Bigg]$$

JHEP07(2024)244

$$\mathcal{A}_{12} = \frac{2p_T^2}{(m_Z^4+p_T^4)}\left[\frac{\left((s'^2-t'^2-u'^2)\,m_Z^2+p_T^2\,(s'^2+t'^2+u'^2)\right)}{(m_Z^2+p_T^2)\,s'}f_1+p_T^2 s'\left(\frac{t'}{u'}f_{10}+\frac{u'}{t'}f_{11}\right)\right] \tag{A.32}$$

$$\mathcal{A}_{13} = \frac{p_T^2}{m_Z^2}\left[\frac{(m_Z^2-p_T^2)\,s'}{2}\left(\frac{f_5}{t'}+\frac{f_6}{u'}\right)-(f_2+f_3+t'f_4+u'f_7)\right] \tag{A.33}$$

$$\mathcal{A}_{14} = -\frac{p_T^2}{m_Z^2}\left[f_2+f_3+p_T^2 s'\left(\frac{f_5}{t'}+\frac{f_6}{u'}\right)\right] \tag{A.34}$$

$$\mathcal{A}_{15} = \frac{p_T^2}{2m_Z^4}\left[\left(m_Z^2+p_T^2\right)(f_2+f_3+t'f_4+u'f_7)-\left(m_Z^2-p_T^2\right)(u'f_5+t'f_6)\right] \tag{A.35}$$

$$\mathcal{A}_{16} = \frac{2p_T^2}{m_Z^2+p_T^2}\left[f_2+f_3+\frac{2p_T^2}{m_Z^2+p_T^2}\,(u'f_5+t'f_6)\right] \tag{A.36}$$

$$\mathcal{A}_{17} = \frac{2m_Z^2}{2m_Z^2+p_T^2}\left[\frac{\left(s'^2\,(t'^2+u'^2)-(t'^2-u'^2)^2\right)}{s'^3\,(m_Z^2+p_T^2)}f_1+f_2+f_3\right] \tag{A.37}$$

$$\mathcal{A}_{18} = \frac{\left(m_Z^2\,(2s'^2-t'^2-u'^2)+s'(s'(p_T^2-s')+t'^2+u'^2)\right)}{m_Z^2 s'\,(m_Z^2+p_T^2)}\left(p_T^2 f_8-f_1\right) \tag{A.38}$$

B Analytical results

Results for double-triangle diagrams. With reference to eq. (2.10), we present here the exact results for the double-triangle contributions to the $\mathcal{A}_i^{(1,\bowtie)}$ with $i=1,\ldots,18$. We keep the dependence of the final result on the mass of the bottom quark, m_b. We find

$$\mathcal{A}_1^{(1,\bowtie)} = 0 \tag{B.1}$$

$$\mathcal{A}_2^{(1,\bowtie)} = \frac{p_T\left((m_Z^2+2t')\;\Delta(t')^2-(t'\leftrightarrow u')\right)}{32\sqrt{2}m_Z\;\;(m_Z^2+p_T^2)} \tag{B.2}$$

$$\mathcal{A}_3^{(1,\bowtie)} = -\frac{p_T^3\left(u'\Delta(t')^2-(t'\leftrightarrow u')\right)}{16\;\sqrt{2}m_Z\,(m_Z^2+p_T^2)^2} \tag{B.3}$$

$$\mathcal{A}_4^{(1,\bowtie)} = 0 \tag{B.4}$$

$$\mathcal{A}_5^{(1,\bowtie)} = -\frac{p_T\;\;(t'\;\Delta(t')^2-(t'\leftrightarrow u'))}{16\sqrt{2}m_Z\;\;(m_Z^2+p_T^2)} \tag{B.5}$$

$$\mathcal{A}_6^{(1,\bowtie)} = -\frac{p_T\left((m_Z^2+2t')\,u'^2\;\Delta(t')^2-(t'\leftrightarrow u')\right)}{16\sqrt{2}m_Z\;\;(m_Z^2+p_T^2)^2\,s'} \tag{B.6}$$

$$\mathcal{A}_7^{(1,\bowtie)} = \frac{\left(s'\;p_T^2+t'^2\right)u'^2\;\Delta(t')^2-(t'\leftrightarrow u')}{16\sqrt{2}\;\;(m_Z^2+p_T^2)^2\,s'^2} \tag{B.7}$$

$$\mathcal{A}_8^{(1,\bowtie)} = \frac{u'\left(t'(m_Z^2+p_T^2)-2s'p_T^2\right)\Delta(t')^2-(t'\leftrightarrow u')}{32\sqrt{2}\;\;(m_Z^2+p_T^2)^2\;\;s'} \tag{B.8}$$

$$\mathcal{A}_9^{(1,\bowtie)} = \frac{(m_Z^2-p_T^2)\left((m_Z^2+2t')\;\;\Delta(t')^2+(t'\leftrightarrow u')\right)}{64m_Z^2\;\sqrt{m_Z^4+p_T^4}} \tag{B.9}$$

$$\mathcal{A}_{10}^{(1,\bowtie)} = -\frac{p_T^2\;\;\left((m_Z^2+2t')\;\;\Delta(t')^2+(t'\leftrightarrow u')\right)}{32\,(m_Z^2+p_T^2)\;\sqrt{m_Z^4+p_T^4}} \tag{B.10}$$

JHEP07(2024)244

$$\mathcal{A}_{11}^{(1,\bowtie)} = \frac{u'\left(m_Z^2+2\ t'\right)\left(2s'\ m_Z^2+\left(m_Z^2+p_T^2\right)\left(t'+2\ u'\right)\right)\Delta(t')^2+(t'\leftrightarrow u')}{32m_Z^2\ \left(m_Z^2+p_T^2\right)\sqrt{m_Z^4+p_T^4}\ s'} \tag{B.11}$$

$$\mathcal{A}_{12}^{(1,\bowtie)} = -\frac{\left(s'm_Z^4+4p_T^2s'\ m_Z^2+3p_T^4s'+4p_T^2\ \left(t'^2+u'^2\right)\right)\ \left(\Delta(t')^2+\Delta(u')^2\right)}{64\ \left(m_Z^2+p_T^2\right)\sqrt{m_Z^4+p_T^4}\ s'} \tag{B.12}$$

$$\mathcal{A}_{13}^{(1,\bowtie)} = \frac{p_T\left(\left(m_Z^2+2t'\right)\ u'^2\Delta(t')^2+(t'\leftrightarrow u')\right)}{16\sqrt{2}m_Z\ \left(m_Z^2+p_T^2\right)^2 s'} \tag{B.13}$$

$$\mathcal{A}_{14}^{(1,\bowtie)} = -\frac{\left(s'\ p_T^2+t'^2\right)u'^2\ \Delta(t')^2+(t'\leftrightarrow u')}{64\sqrt{2}\ \left(m_Z^2+p_T^2\right)^2 s'^2} \tag{B.14}$$

$$\mathcal{A}_{15}^{(1,\bowtie)} = -\frac{p_T\ \left(\left(m_Z^2+2t'\right)u'^2\ \Delta(t')^2+(t'\leftrightarrow u')\right)}{16\sqrt{2}m_Z\ \left(m_Z^2+p_T^2\right)^2 s'} \tag{B.15}$$

$$\mathcal{A}_{16}^{(1,\bowtie)} = \frac{\left(s'\ p_T^2+t'^2\right)u'^2\ \Delta(t')^2+(t'\leftrightarrow u')}{16\sqrt{2}\ \left(m_Z^2+p_T^2\right)^2 s'^2} \tag{B.16}$$

$$\mathcal{A}_{17}^{(1,\bowtie)} = 0 \tag{B.17}$$

$$\mathcal{A}_{18}^{(1,\bowtie)} = \frac{1}{64}\left(\left(\frac{s'\ p_T^2}{t'^2}+1\right)\ \Delta(t')^2+(t'\leftrightarrow u')\right) \tag{B.18}$$

where

$$\Delta(x) = F(x,m_t) - F(x,m_b) \tag{B.19}$$

and

$$\begin{aligned} F(x,M) = \frac{m_Z^2}{x}\Big[B_0(2x+m_Z^2,M^2,M^2) - B_0(m_Z^2,M^2,M^2)\Big] \\ + 4M^2C_0(0,m_Z^2,2x+m_Z^2,M^2,M^2,M^2) + 2 \end{aligned} \tag{B.20}$$

Results for triangle diagrams at NLO. With reference to eq. (2.10), we present here the exact results for the two-loop one-particle-irreducible triangle contributions to the NLO form factors. We obtain

$$\mathcal{A}_1^{(1,\triangle)} = 0 \tag{B.21}$$

$$\mathcal{A}_2^{(1,\triangle)} = \frac{p_T^2(\hat{t}-\hat{u})}{m_Z^2(p_T^2+m_Z^2)}\frac{\hat{s}}{\hat{s}-m_H^2}\left(C_F\mathcal{F}_{1/2}^{(2l)}+C_A\mathcal{G}_{1/2}^{(2l,CA)}\right) \tag{B.22}$$

$$\mathcal{A}_3^{(1,\triangle)} = 0 \tag{B.23}$$

$$\mathcal{A}_4^{(1,\triangle)} = 0 \tag{B.24}$$

$$\mathcal{A}_5^{(1,\triangle)} = -\frac{p_T^2(\hat{t}-\hat{u})}{m_Z^2(p_T^2+m_Z^2)}\frac{\hat{s}}{\hat{s}-m_H^2}\left(C_F\mathcal{F}_{1/2}^{(2l)}+C_A\mathcal{G}_{1/2}^{(2l,CA)}\right) \tag{B.25}$$

$$\mathcal{A}_6^{(1,\triangle)} = 0 \tag{B.26}$$

$$\mathcal{A}_7^{(1,\triangle)} = 0 \tag{B.27}$$

$$\mathcal{A}_8^{(1,\triangle)} = 0 \tag{B.28}$$

$$\mathcal{A}_9^{(1,\triangle)} = \frac{\hat{s}(p_T^2-m_Z^2)+2m_Z^2(p_T^2+m_Z^2)}{2m_Z^4}\frac{\hat{s}}{\hat{s}-m_H^2}\left(C_F\mathcal{F}_{1/2}^{(2l)}+C_A\mathcal{G}_{1/2}^{(2l,CA)}\right) \tag{B.29}$$

JHEP07(2024)244

$$\mathcal{A}_{10}^{(1,\triangle)} = \frac{2p_T^2(p_T^2\hat{s}+m_Z^4-p_T^4)}{(p_T^2+m_Z^2)(p_T^4+m_Z^4)}\frac{\hat{s}}{\hat{s}-m_H^2}\left(C_F\mathcal{F}_{1/2}^{(2l)}+C_A\mathcal{G}_{1/2}^{(2l,CA)}\right) \tag{B.30}$$

$$\mathcal{A}_{11}^{(1,\triangle)} = -\frac{(\hat{s}(p_T^2-m_Z^2)+2m_Z^2(p_T^2+m_Z^2)}{2m_Z^4}\frac{\hat{s}}{\hat{s}-m_H^2}\left(C_F\mathcal{F}_{1/2}^{(2l)}+C_A\mathcal{G}_{1/2}^{(2l,CA)}\right) \tag{B.31}$$

$$\mathcal{A}_{12}^{(1,\triangle)} = -\frac{2p_T^2(p_T^2\hat{s}+m_Z^4-p_T^4)}{(p_T^2+m_Z^2)(p_T^4+m_Z^4)}\frac{\hat{s}}{\hat{s}-m_H^2}\left(C_F\mathcal{F}_{1/2}^{(2l)}+C_A\mathcal{G}_{1/2}^{(2l,CA)}\right) \tag{B.32}$$

$$\mathcal{A}_{13}^{(1,\triangle)} = 0 \tag{B.33}$$

$$\mathcal{A}_{14}^{(1,\triangle)} = 0 \tag{B.34}$$

$$\mathcal{A}_{15}^{(1,\triangle)} = 0 \tag{B.35}$$

$$\mathcal{A}_{16}^{(1,\triangle)} = 0 \tag{B.36}$$

$$\mathcal{A}_{17}^{(1,\triangle)} = -\frac{2m_Z^2}{p_T^2+2m_Z^2}\frac{\hat{s}}{\hat{s}-m_H^2}\left(C_F\mathcal{F}_{1/2}^{(2l)}+C_A\mathcal{G}_{1/2}^{(2l,CA)}\right) \tag{B.37}$$

$$\mathcal{A}_{18}^{(1,\triangle)} = \frac{\hat{s}}{\hat{s}-m_H^2}\left(C_F\mathcal{F}_{1/2}^{(2l)}+C_A\mathcal{G}_{1/2}^{(2l,CA)}\right) \tag{B.38}$$

where the functions $\mathcal{F}_{1/2}^{(2l)}$ and $\mathcal{G}_{1/2}^{(2l,CA)}$ are defined in eqs. (2.11) and (3.8) in ref. [34].

References

[1] ATLAS collaboration, *A detailed map of Higgs boson interactions by the ATLAS experiment ten years after the discovery*, *Nature* **607** (2022) 52 [*Erratum ibid.* **612** (2022) E24] [arXiv:2207.00092] [INSPIRE].

[2] CMS collaboration, *A portrait of the Higgs boson by the CMS experiment ten years after the discovery*, *Nature* **607** (2022) 60 [arXiv:2207.00043] [INSPIRE].

[3] G. Heinrich, *Collider Physics at the Precision Frontier*, *Phys. Rept.* **922** (2021) 1 [arXiv:2009.00516] [INSPIRE].

[4] A. Huss, J. Huston, S. Jones and M. Pellen, *Les Houches 2021 — physics at TeV colliders: report on the standard model precision wishlist*, *J. Phys. G* **50** (2023) 043001 [arXiv:2207.02122] [INSPIRE].

[5] ATLAS collaboration, *Evidence of pair production of longitudinally polarised vector bosons and study of CP properties in $ZZ \to 4\ell$ events with the ATLAS detector at $\sqrt{s} = 13$ TeV*, *JHEP* **12** (2023) 107 [arXiv:2310.04350] [INSPIRE].

[6] ATLAS collaboration, *Measurement of ZZ production cross-sections in the four-lepton final state in pp collisions at $\sqrt{s} = 13.6$ TeV with the ATLAS experiment*, *Phys. Lett. B* **855** (2024) 138764 [arXiv:2311.09715] [INSPIRE].

[7] R.W. Brown and K.O. Mikaelian, *W^+W^- and Z^0Z^0 Pair Production in $e^+e^-, pp, p\bar{p}$ Colliding Beams*, *Phys. Rev. D* **19** (1979) 922 [INSPIRE].

JHEP07(2024)244

[8] J. Ohnemus and J.F. Owens, *An order-α_s calculation of hadronic ZZ production*, *Phys. Rev. D* **43** (1991) 3626 [INSPIRE].

[9] B. Mele, P. Nason and G. Ridolfi, *QCD radiative corrections to Z boson pair production in hadronic collisions*, *Nucl. Phys. B* **357** (1991) 409 [INSPIRE].

[10] F. Cascioli et al., *ZZ production at hadron colliders in NNLO QCD*, *Phys. Lett. B* **735** (2014) 311 [arXiv:1405.2219] [INSPIRE].

[11] T. Gehrmann, A. von Manteuffel, L. Tancredi and E. Weihs, *The two-loop master integrals for $q\bar{q} \to VV$*, *JHEP* **06** (2014) 032 [arXiv:1404.4853] [INSPIRE].

[12] F. Caola et al., *Two-loop helicity amplitudes for the production of two off-shell electroweak bosons in quark-antiquark collisions*, *JHEP* **11** (2014) 041 [arXiv:1408.6409] [INSPIRE].

[13] T. Gehrmann, A. von Manteuffel and L. Tancredi, *The two-loop helicity amplitudes for $q\bar{q}' \to V_1V_2 \to 4$ leptons*, *JHEP* **09** (2015) 128 [arXiv:1503.04812] [INSPIRE].

[14] E. Accomando, A. Denner and A. Kaiser, *Logarithmic electroweak corrections to gauge-boson pair production at the LHC*, *Nucl. Phys. B* **706** (2005) 325 [hep-ph/0409247] [INSPIRE].

[15] A. Bierweiler, T. Kasprzik and J.H. Kühn, *Vector-boson pair production at the LHC to $\mathcal{O}(\alpha^3)$ accuracy*, *JHEP* **12** (2013) 071 [arXiv:1305.5402] [INSPIRE].

[16] J. Baglio, L.D. Ninh and M.M. Weber, *Massive gauge boson pair production at the LHC: a next-to-leading order story*, *Phys. Rev. D* **88** (2013) 113005 [*Erratum ibid.* **94** (2016) 099902] [arXiv:1307.4331] [INSPIRE].

[17] M. Grazzini, S. Kallweit, M. Wiesemann and J.Y. Yook, *ZZ production at the LHC: NLO QCD corrections to the loop-induced gluon fusion channel*, *JHEP* **03** (2019) 070 [arXiv:1811.09593] [INSPIRE].

[18] D.A. Dicus, C. Kao and W.W. Repko, *Gluon Production of Gauge Bosons*, *Phys. Rev. D* **36** (1987) 1570 [INSPIRE].

[19] E.W.N. Glover and J.J. van der Bij, *Z-boson pair production via gluon fusion*, *Nucl. Phys. B* **321** (1989) 561 [INSPIRE].

[20] ATLAS collaboration, *Constraints on off-shell Higgs boson production and the Higgs boson total width in $ZZ \to 4\ell$ and $ZZ \to 2\ell 2\nu$ final states with the ATLAS detector*, *Phys. Lett. B* **786** (2018) 223 [arXiv:1808.01191] [INSPIRE].

[21] CMS collaboration, *Measurements of the Higgs boson width and anomalous HVV couplings from on-shell and off-shell production in the four-lepton final state*, *Phys. Rev. D* **99** (2019) 112003 [arXiv:1901.00174] [INSPIRE].

[22] F. Caola and K. Melnikov, *Constraining the Higgs boson width with ZZ production at the LHC*, *Phys. Rev. D* **88** (2013) 054024 [arXiv:1307.4935] [INSPIRE].

[23] J.M. Campbell, R.K. Ellis and C. Williams, *Bounding the Higgs Width at the LHC Using Full Analytic Results for $gg \to e^-e^+\mu^-\mu^+$*, *JHEP* **04** (2014) 060 [arXiv:1311.3589] [INSPIRE].

[24] E. Balzani, R. Gröber and M. Vitti, *Light-quark Yukawa couplings from off-shell Higgs production*, *JHEP* **10** (2023) 027 [arXiv:2304.09772] [INSPIRE].

[25] U. Haisch and G. Koole, *Off-shell Higgs production at the LHC as a probe of the trilinear Higgs coupling*, *JHEP* **02** (2022) 030 [arXiv:2111.12589] [INSPIRE].

[26] U. Haisch and G. Koole, *Probing Higgs portals with matrix-element based kinematic discriminants in $ZZ \to 4\ell$ production*, *JHEP* **04** (2022) 166 [arXiv:2201.09711] [INSPIRE].

JHEP07(2024)244

[27] U. Haisch, M. Ruhdorfer, K. Schmid and A. Weiler, *Quantum collider probes of the fermionic Higgs portal*, *SciPost Phys.* **16** (2024) 112 [arXiv:2311.03995] [INSPIRE].

[28] N. Kauer and G. Passarino, *Inadequacy of zero-width approximation for a light Higgs boson signal*, *JHEP* **08** (2012) 116 [arXiv:1206.4803] [INSPIRE].

[29] C. Englert and M. Spannowsky, *Limitations and Opportunities of Off-Shell Coupling Measurements*, *Phys. Rev. D* **90** (2014) 053003 [arXiv:1405.0285] [INSPIRE].

[30] C. Englert, Y. Soreq and M. Spannowsky, *Off-Shell Higgs Coupling Measurements in BSM scenarios*, *JHEP* **05** (2015) 145 [arXiv:1410.5440] [INSPIRE].

[31] CMS collaboration, *Measurement of the Higgs boson width and evidence of its off-shell contributions to ZZ production*, *Nature Phys.* **18** (2022) 1329 [arXiv:2202.06923] [INSPIRE].

[32] ATLAS collaboration, *Evidence of off-shell Higgs boson production from ZZ leptonic decay channels and constraints on its total width with the ATLAS detector*, *Phys. Lett. B* **846** (2023) 138223 [arXiv:2304.01532] [INSPIRE].

[33] C. Anastasiou et al., *Two-loop amplitudes and master integrals for the production of a Higgs boson via a massive quark and a scalar-quark loop*, *JHEP* **01** (2007) 082 [hep-ph/0611236] [INSPIRE].

[34] U. Aglietti, R. Bonciani, G. Degrassi and A. Vicini, *Analytic Results for Virtual QCD Corrections to Higgs Production and Decay*, *JHEP* **01** (2007) 021 [hep-ph/0611266] [INSPIRE].

[35] R. Harlander and P. Kant, *Higgs production and decay: Analytic results at next-to-leading order QCD*, *JHEP* **12** (2005) 015 [hep-ph/0509189] [INSPIRE].

[36] A. von Manteuffel and L. Tancredi, *The two-loop helicity amplitudes for $gg \to V_1V_2 \to 4$ leptons*, *JHEP* **06** (2015) 197 [arXiv:1503.08835] [INSPIRE].

[37] F. Caola, K. Melnikov, R. Röntsch and L. Tancredi, *QCD corrections to ZZ production in gluon fusion at the LHC*, *Phys. Rev. D* **92** (2015) 094028 [arXiv:1509.06734] [INSPIRE].

[38] K. Melnikov and M. Dowling, *Production of two Z-bosons in gluon fusion in the heavy top quark approximation*, *Phys. Lett. B* **744** (2015) 43 [arXiv:1503.01274] [INSPIRE].

[39] F. Caola et al., *QCD corrections to vector boson pair production in gluon fusion including interference effects with off-shell Higgs at the LHC*, *JHEP* **07** (2016) 087 [arXiv:1605.04610] [INSPIRE].

[40] J.M. Campbell, R.K. Ellis, M. Czakon and S. Kirchner, *Two loop correction to interference in $gg \to ZZ$*, *JHEP* **08** (2016) 011 [arXiv:1605.01380] [INSPIRE].

[41] R. Gröber, A. Maier and T. Rauh, *Top quark mass effects in $gg \to ZZ$ at two loops and off-shell Higgs boson interference*, *Phys. Rev. D* **100** (2019) 114013 [arXiv:1908.04061] [INSPIRE].

[42] J. Davies, G. Mishima, M. Steinhauser and D. Wellmann, *$gg \to ZZ$: analytic two-loop results for the low- and high-energy regions*, *JHEP* **04** (2020) 024 [arXiv:2002.05558] [INSPIRE].

[43] B. Agarwal, S.P. Jones and A. von Manteuffel, *Two-loop helicity amplitudes for $gg \to ZZ$ with full top-quark mass effects*, *JHEP* **05** (2021) 256 [arXiv:2011.15113] [INSPIRE].

[44] C. Brønnum-Hansen and C.-Y. Wang, *Top quark contribution to two-loop helicity amplitudes for Z boson pair production in gluon fusion*, *JHEP* **05** (2021) 244 [arXiv:2101.12095].

[45] B. Agarwal, S. Jones, M. Kerner and A. von Manteuffel, *Complete NLO QCD Corrections to ZZ Production in Gluon Fusion*, arXiv:2404.05684 [INSPIRE].

JHEP07(2024)244

[46] R. Bonciani, G. Degrassi, P.P. Giardino and R. Gröber, *Analytical Method for Next-to-Leading-Order QCD Corrections to Double-Higgs Production*, *Phys. Rev. Lett.* **121** (2018) 162003 [arXiv:1806.11564] [INSPIRE].

[47] L. Alasfar et al., *Virtual corrections to $gg \to ZH$ via a transverse momentum expansion*, *JHEP* **05** (2021) 168 [arXiv:2103.06225] [INSPIRE].

[48] L. Bellafronte et al., *Gluon fusion production at NLO: merging the transverse momentum and the high-energy expansions*, *JHEP* **07** (2022) 069 [arXiv:2202.12157] [INSPIRE].

[49] J. Davies, G. Mishima, K. Schönwald and M. Steinhauser, *Analytic approximations of $2 \to 2$ processes with massive internal particles*, *JHEP* **06** (2023) 063 [arXiv:2302.01356] [INSPIRE].

[50] F. Caola et al., *Two-loop helicity amplitudes for the production of two off-shell electroweak bosons in gluon fusion*, *JHEP* **06** (2015) 129 [arXiv:1503.08759] [INSPIRE].

[51] T. Hahn, *Generating Feynman diagrams and amplitudes with FeynArts 3*, *Comput. Phys. Commun.* **140** (2001) 418 [hep-ph/0012260] [INSPIRE].

[52] V. Shtabovenko, R. Mertig and F. Orellana, *FeynCalc 9.3: New features and improvements*, *Comput. Phys. Commun.* **256** (2020) 107478 [arXiv:2001.04407] [INSPIRE].

[53] R. Mertig, M. Bohm and A. Denner, *FEYN CALC: Computer algebraic calculation of Feynman amplitudes*, *Comput. Phys. Commun.* **64** (1991) 345 [INSPIRE].

[54] R.N. Lee, *LiteRed 1.4: a powerful tool for reduction of multiloop integrals*, *J. Phys. Conf. Ser.* **523** (2014) 012059 [arXiv:1310.1145] [INSPIRE].

[55] R.N. Lee, *Presenting LiteRed: a tool for the Loop InTEgrals REDuction*, arXiv:1212.2685 [INSPIRE].

[56] G. Passarino and M.J.G. Veltman, *One Loop Corrections for e^+e^- Annihilation Into $\mu^+\mu^-$ in the Weinberg Model*, *Nucl. Phys. B* **160** (1979) 151 [INSPIRE].

[57] R. Bonciani, P. Mastrolia and E. Remiddi, *Vertex diagrams for the QED form-factors at the two loop level*, *Nucl. Phys. B* **661** (2003) 289 [hep-ph/0301170] [INSPIRE].

[58] M. Becchetti and R. Bonciani, *Two-Loop Master Integrals for the Planar QCD Massive Corrections to Di-photon and Di-jet Hadro-production*, *JHEP* **01** (2018) 048 [arXiv:1712.02537] [INSPIRE].

[59] S. Caron-Huot and J.M. Henn, *Iterative structure of finite loop integrals*, *JHEP* **06** (2014) 114 [arXiv:1404.2922] [INSPIRE].

[60] A. von Manteuffel and L. Tancredi, *A non-planar two-loop three-point function beyond multiple polylogarithms*, *JHEP* **06** (2017) 127 [arXiv:1701.05905] [INSPIRE].

[61] L. Naterop, A. Signer and Y. Ulrich, *handyG —Rapid numerical evaluation of generalised polylogarithms in Fortran*, *Comput. Phys. Commun.* **253** (2020) 107165 [arXiv:1909.01656] [INSPIRE].

[62] R. Bonciani, G. Degrassi, P.P. Giardino and R. Gröber, *A Numerical Routine for the Crossed Vertex Diagram with a Massive-Particle Loop*, *Comput. Phys. Commun.* **241** (2019) 122 [arXiv:1812.02698] [INSPIRE].

[63] G. Degrassi, P.P. Giardino and R. Gröber, *On the two-loop virtual QCD corrections to Higgs boson pair production in the Standard Model*, *Eur. Phys. J. C* **76** (2016) 411 [arXiv:1603.00385] [INSPIRE].

JHEP07(2024)244

[64] R. Gröber, A. Maier and T. Rauh, *Reconstruction of top-quark mass effects in Higgs pair production and other gluon-fusion processes*, *JHEP* **03** (2018) 020 [arXiv:1709.07799] [INSPIRE].

[65] E. Bagnaschi, G. Degrassi and R. Gröber, *Higgs boson pair production at NLO in the POWHEG approach and the top quark mass uncertainties*, *Eur. Phys. J. C* **83** (2023) 1054 [arXiv:2309.10525] [INSPIRE].

[66] J. Baglio et al., *Gluon fusion into Higgs pairs at NLO QCD and the top mass scheme*, *Eur. Phys. J. C* **79** (2019) 459 [arXiv:1811.05692] [INSPIRE].

[67] J. Baglio et al., $gg \to HH$*: Combined uncertainties*, *Phys. Rev. D* **103** (2021) 056002 [arXiv:2008.11626] [INSPIRE].

[68] G. Degrassi, R. Gröber, M. Vitti and X. Zhao, *On the NLO QCD corrections to gluon-initiated ZH production*, *JHEP* **08** (2022) 009 [arXiv:2205.02769] [INSPIRE].

[69] D. Binosi and L. Theussl, *JaxoDraw: A graphical user interface for drawing Feynman diagrams*, *Comput. Phys. Commun.* **161** (2004) 76 [hep-ph/0309015] [INSPIRE].

JHEP07(2024)244